Key Points:
- An under-ice phytoplankton bloom developed during June–July in the northeast Chukchi Sea within the Central Channel flow branch
- A plume of chlorophyll fluorescence extending downwards from the bloom along the current's water mass front was continually present
- A simple numerical model demonstrates that the plume is the result of baroclinic instability of the frontal jet

Author Contributions:

Conceptualization: Robert S. Pickart, Michael A. Spall, Matthew Mills, Kevin R. Arrigo, Gert van Dijken
Data curation: Leah T. McRaven
Formal analysis: Robert S. Pickart, Michael A. Spall, Loreley Lago, Peigen Lin, Astrid Pacini, Jie Huang
Methodology: Frank Bahr, Loreley Lago, Peigen Lin, Astrid Pacini, Matthew Mills, Jie Huang, Kevin R. Arrigo, Gert van Dijken, Steven Roberts
Software: Steven Roberts
Writing – original draft: Robert S. Pickart, Michael A. Spall

Vertical Carbon Export During a Phytoplankton Bloom in the Chukchi Sea: Physical Setting and Frontal Subduction

Robert S. Pickart[1] ⓘ**, Michael A. Spall[1], Frank Bahr[1], Loreley Lago[1], Peigen Lin[1,2]** ⓘ**, Astrid Pacini[3]** ⓘ**, Matthew Mills[4], Jie Huang[1]** ⓘ**, Kevin R. Arrigo[4]** ⓘ**, Gert van Dijken[4], Leah T. McRaven[1]** ⓘ**, and Steven Roberts[5]**

[1]Woods Hole Oceanographic Institution, Woods Hole, MA, USA, [2]Shanghai Jiao Tong University, School of Oceanography, Shanghai, China, [3]Applied Physics Laboratory, Polar Science Center, University of Washington, Seattle, WA, USA, [4]Department of Earth System Science, Stanford University, Stanford, CA, USA, [5]University of Alaska Fairbanks, School of Fisheries and Ocean Sciences, Seward Marine Center, Fairbanks, AK, USA

Abstract In order to quantify pelagic-benthic coupling on high-latitude shelves, it is imperative to identify the different physical mechanisms by which phytoplankton are exported to the sediments. In June–July 2023, a field program documented the evolution of an under-ice phytoplankton bloom on the northeast Chukchi shelf. Here, we use in situ data from the cruise, a simple numerical model, historical water column data, and ocean reanalysis fields to characterize the physical setting and describe the dynamically driven vertical export of chlorophyll associated with the bloom. A water mass front separating cold, high-nutrient winter water in the north and warmer summer waters to the south—roughly coincident with the ice edge—supported a baroclinic jet which is part of the Central Channel flow branch that veers eastward toward Barrow Canyon. A plume of high chlorophyll fluorescence extending from the near-surface bloom in the winter water downwards along the front was measured throughout the cruise. Using a passive tracer to represent phytoplankton in the model, it was demonstrated that the plume is the result of subduction due to baroclinic instability of the frontal jet. This process, in concert with the gravitational sinking, pumps the chlorophyll downwards an order of magnitude faster than gravitational sinking alone. Particle tracking using the ocean reanalysis fields reveals that a substantial portion of the chlorophyll away from the front is advected off of the northeast Chukchi shelf before reaching the bottom. This highlights the importance of the frontal subduction process for delivering carbon to the sea floor.

Plain Language Summary The Chukchi Sea shelf north of Bering Strait is known to experience some of the largest phytoplankton blooms in the Arctic Ocean. In 2023, a field program was carried out to quantify aspects of the early summer bloom, with an emphasis on characterizing how the phytoplankton biomass from the bloom is exported to the sea floor. A large bloom was measured under the pack ice in very cold, high-nutrient water, just north of warmer, ice-free waters. The front separating the warm and cold waters supported a current flowing eastward, which is one of the main flow pathways on the Chukchi shelf. A plume of high chlorophyll fluorescence extending from the near-surface bloom downwards along the front was measured throughout the cruise. We demonstrate that this vertical pumping was due to a dynamical process associated with the current which resulted in much faster downward export of phytoplankton than gravitational sinking alone. Tracking the fate of particles on the northeast Chukchi shelf using an ocean simulation revealed that much of the phytoplankton biomass away from the front is carried off the shelf before reaching the bottom. This highlights the importance of the frontal process for delivering chlorophyll to the sea floor.

1. Introduction

The Chukchi Sea shelf north of Bering Strait has one of the highest rates of primary production anywhere in the Arctic Ocean (Hill et al., 2018; Springer & McRoY, 1993; Varela et al., 2013). This is in part due to the dramatic loss of sea ice cover in recent decades (Frey et al., 2014), resulting in more extensive open water phytoplankton blooms (Arrigo & van Dijken, 2015). At the same time, the decrease in early season sea ice thickness on the Chukchi shelf, together with a greater preponderance of leads and melt-ponds, has resulted in significant under-ice blooms (Arrigo et al., 2012; Lowry et al., 2014; Perovich & Polashenski, 2012). One contributor to this is the greater availability of nutrients across the shelf earlier in the spring, since the high-nutrient winter water has not yet drained through Barrow Canyon (Lin et al., 2019; Shroyer & Pickart, 2019). The high production on the

Writing – review & editing: Frank Bahr, Loreley Lago, Peigen Lin, Astrid Pacini, Matthew Mills, Jie Huang, Kevin R. Arrigo, Gert van Dijken, Steven Roberts

Chukchi shelf in turn impacts the rest of the food web, including zooplankton, fish, marine mammals, and seabirds (De Robertis et al., 2017; Ershova et al., 2015; Kuletz et al., 2015; Logerwell et al., 2015; Moore & Kuletz, 2019). It also results in significant vertical carbon export to the benthos, which supports high levels of benthic activity (Grebmeier et al., 2006, 2015).

Presently it is uncertain how the pelagic-benthic coupling on the Chukchi shelf will respond to the continued loss and thinning of the ice cover. To help determine this, it is important to identify the different physical mechanisms, aside from gravitational sinking, by which phytoplankton are exported to the sediments, and if there are particular geographical regions where such export is stronger. One well known benthic hotspot exists in the center of Barrow Canyon on the northeast Chukchi shelf (Grebmeier et al., 2015). Pickart et al. (2021) demonstrated that this region of locally enhanced macrofaunal benthic biomass is likely due to strong downwelling as a result of the convergent northward flow into the canyon. However, this physical mechanism applies only to this single geographical location where the lateral flow convergence is especially strong due to the bathymetry of the canyon. It is of interest to know if other dynamical processes, more generic to the Chukchi shelf, are able to efficiently transport phytoplankton to depth.

One possible process is subduction, by which fluid parcels are transferred from the surface mixed layer into the interior of the water column. On large-scales, subduction can be forced by Ekman pumping or lateral advection through the base of a sloping mixed layer depth (Marshall et al., 1993). On small-scales on the order of 10 km, subduction can be forced by frontal dynamics and mesoscale and submesoscale eddies (Marshall, 1997; Spall, 1995). The ageostrophic circulation that drives subduction arises in regions of frontogenesis, where parcels undergo an acceleration as they flow into regions of convergence along the front (Hoskins & Bretherton, 1972). Subduction events can be transient and localized, as might be found when two eddies interact, or they can be more persistent in regions where an unstable front is maintained by a large-scale deformation field (Spall, 1997).

Both observations and models indicate that frontal regions can be very effective locations for the transport of tracers (heat, salt, chlorophyll, carbon, oxygen, etc.) between the upper layer and the deeper ocean (e.g., Marshall, 1997; Pollard & Regier, 1992; Ruiz et al., 2019; Thomas & Joyce, 2010). On the Chukchi shelf, fronts exist on different scales and at different times of the year. During ice retreat in the spring, meltwater fronts arise between the newly melted cold water and warmer waters to the south (Lu et al., 2015; Weingartner et al., 2017). These fronts are confined to the near-surface layer and have been shown to be baroclinically unstable, leading to eddy formation and lateral fluxes of heat (Lu et al., 2015). Deeper-reaching hydrographic fronts are associated with the three main flow branches on the Chukchi shelf: the western pathway progressing into Herald Canyon, the Central Channel pathway, and the Alaskan coastal current (ACC) (Figure 1). These fronts are referred to as water mass fronts, as they are associated with the different types of summer and winter waters flowing northward through Bering Strait. While the properties and kinematics of the three Chukchi Sea flow branches have been studied extensively through the years via observations and models (e.g., Pickart et al., 2010, 2016; Spall, 2007; Weingartner et al., 2017; Woodgate et al., 2005), little is known about the stability characteristics of their associated water mass fronts.

In summer of 2023, a field program was carried out to further our understanding of the vertical export of carbon associated with the three different types of microalgal blooms that occur on the Chukchi shelf during the transition from late-spring to early summer: the ice algal bloom; the under-ice water column bloom; and the marginal ice/open-water bloom. In this study, we use the shipboard hydrographic and velocity data, together with a simple numerical model and ocean state reanalysis fields, to investigate the dynamics by which the phytoplankton are transported to depth in conjunction with the water mass front of the Central Channel flow branch as well as the ultimate fate of the phytoplankton. We begin by describing the general physical setting and how it evolved over the course of the cruise, then present aspects of the bloom development. Next, we identify and diagnose the downward pumping that arises through frontal subduction associated with baroclinic instability, and, finally, we demonstrate the importance of this mechanism versus gravitational sinking alone in supplying carbon to the benthos of the Chukchi shelf.

2. Data and Methods

From 16 June to 30 July 2023, a cruise aboard R/V *Sikuliaq* was carried out as part of the program entitled "The Tale of Three Systems: Fate of primary production in the Chukchi Sea." The study area is north of Icy Cape and south of Hanna Shoal, in the region where parts of the Central Channel pathway veer to the east toward Barrow
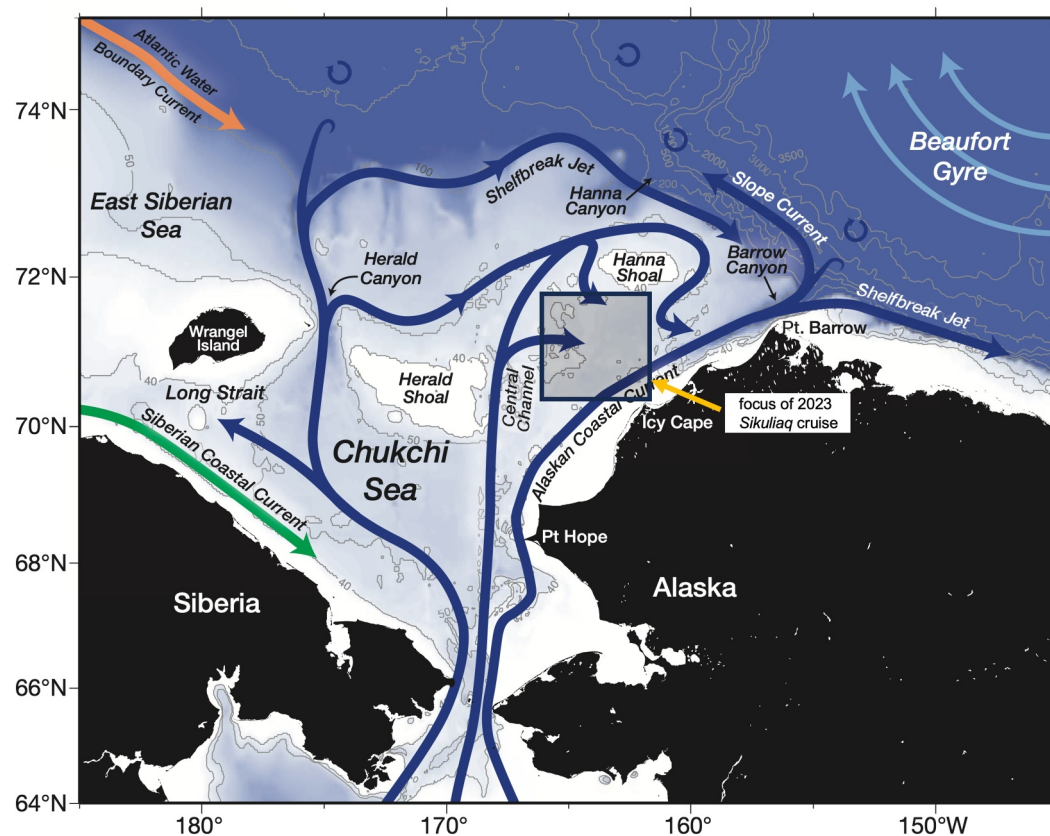
Figure 1. Schematic circulation of the Chukchi Sea with place names (after Corlett & Pickart, 2017). The box denotes the study region. The bottom topography (in meters) is from ETOPO-2.

Canyon (Figure 1). Over the course of the cruise, we did seven complete circuits of a polygon, hereafter referred to as the "box" (Figure 2). The rationale for the location of the box is given in the next section. Other transects farther to the south were done as well on the cruise, which will be considered in future studies.

2.1. Hydrographic Data

A total of 300 conductivity-temperature-depth (CTD) casts were done over the 45-day cruise using a Sea-Bird 911+ system measuring pressure (Digiquartz), dual temperature/conductivity (SBE3/SBE4), oxygen (SBE43), beam transmission (WET Labs C-Star), fluorescence (WET Labs ECO-AFL/FL), and photosynthetically active radiation (Biospherical QSP2300). The CTD system was mounted on a 24-position rosette with 10-L Niskin bottles. In this study, we use the CTD temperature, salinity, fluorescence, and photosynthetically active radiation data. The SBE3/SBE4 sensors were calibrated at Sea-Bird prior to and following *Sikuliaq's* field season. The accuracy of the temperature is 0.001°C. Because the cruise took place entirely in shallow water (<60 m), no bottle salinity samples were taken. Based on a regression of the dual conductivity sensors, the accuracy of the salinity is taken to be 0.009 (practical salinity). This is more than accurate enough to capture the signals of interest in the study region.

The fluorometer recorded vertical profiles of chlorophyll *a* (Chl *a*) fluorescence, an indicator of active phytoplankton biomass and Chl *a* concentrations. Prior to the cruise, a scale factor for the sensor was determined by the manufacturer using a mono-culture of phytoplankton (*Thalassiosira weissflogii*). Since the relationship between fluorescence and Chl *a* is highly variable, this scale factor is appropriate for approximate/relative values of Chl *a* fluorescence but cannot be used to determine absolute Chl *a* concentration values. As with the salinity, the signals of interest for fluorescence in this study are clearly captured.
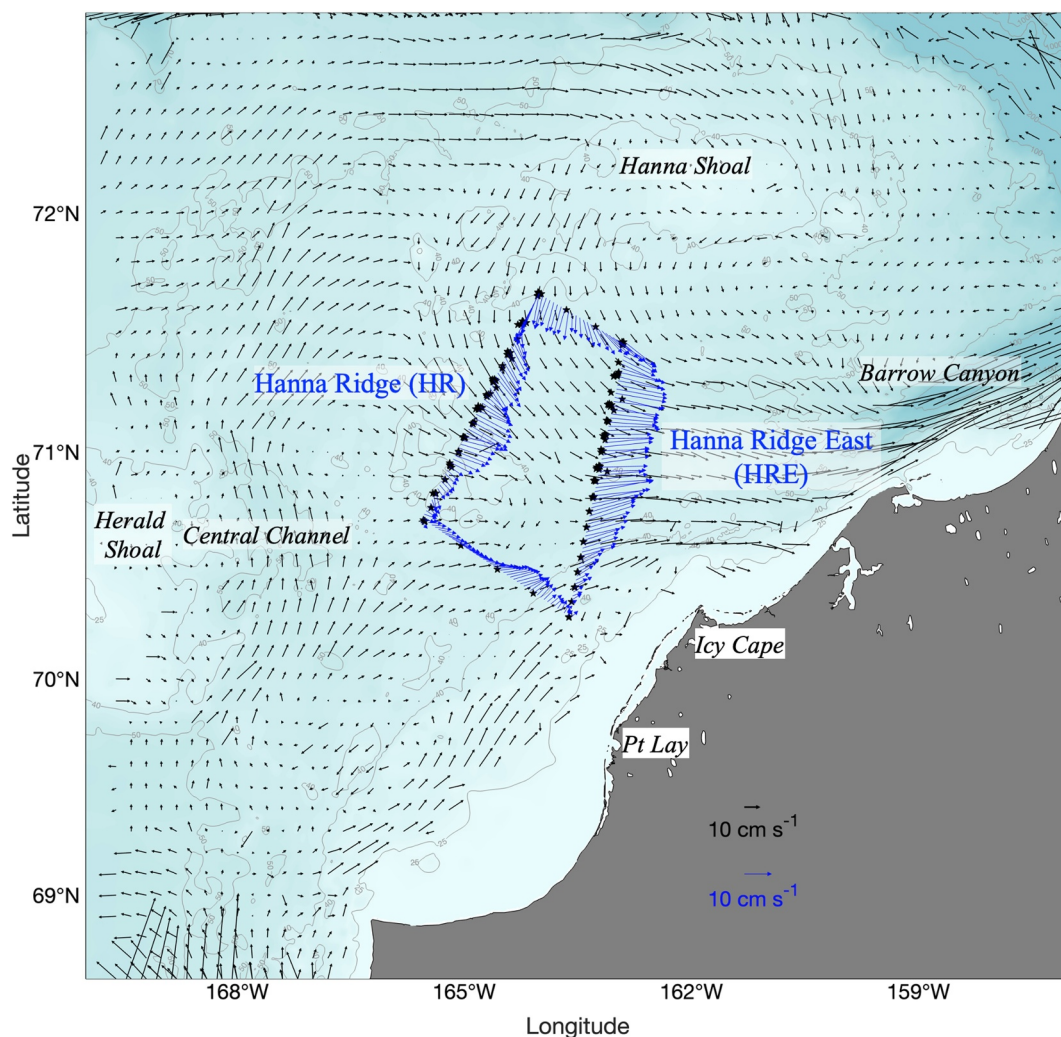
Figure 2. CTD stations (back stars) comprising the repeat occupations of the box. The focus of the study is on the two quasi-meridional sections: Hanna Ridge and Hanna Ridge East. The black vectors are the depth-mean flow from the ChukSA climatology. The blue vectors are the depth-mean flow from Sikuliaq's shipboard acoustic Doppler current profiler, averaged over the seven occupations of the box (see Section 3.2 for details). Note the different scales in the legend. The bottom topography (color and gray contours, in meters) is from IBCAO v3.

Because of the calm conditions experienced throughout the cruise, the CTD was typically lowered to within 1–2 m of the sea floor. The final processed CTD data files are 1-dbar averaged downcast files where a small number of density spikes >0.02 kg m^{-3} were removed and interpolated over.

As mentioned above, we occupied the box seven times during the cruise. The analysis here focuses on the two quasi-meridional sides of the box. The western section is called Hanna Ridge (HR) since it is located along the corrugated ridge between Hanna Shoal and Herald Shoal (Figure 2). The eastern section is referred to as Hanna Ridge East (HRE). The factors that went into choosing the location of the box were as follows: (a) we wanted the northern portion of the box to be in fully consolidated ice and the southern portion to be in open water, thus crossing the marginal ice zone twice during each circuit; (b) since *Sikuliaq* is designed to operate in medium first year ice, we needed to find an area on the shelf where the ice was not too concentrated/thick to prohibit us from progressing well into the ice-pack at a reasonably fast steaming speed (our first attempt at such a section, to the east of Icy Cape, proved too difficult in this regard); and (c) the box needed to be small enough that we could occupy it numerous times and also that we could launch and recover drifting sediment traps without straying too far from the box. The sediment trap data will be analyzed as part of a future study. On average it took 4.5 days to

complete one circuit of the box; the first occupation of the box did not extend quite as far northward as the others due to particularly consolidated ice.

Vertical sections of the CTD variables were constructed using Laplacian-Spline interpolation with a typical grid spacing of 7.5 km in distance and 2.5 m in depth. The variables plotted were potential temperature, potential density (both referenced to the sea surface, hereafter referred to simply as temperature and density), salinity, and fluorescence. The bottom topography along the ship track was obtained from *Sikuliaq's* echosounder where the data were soundspeed-corrected and smoothed. A standard grid was created for the HR and HRE lines, allowing us to compute average sections and anomaly sections.

2.2. Shipboard Velocity Data

We use water column velocity data from *Sikuliaq's* hull-mounted acoustic Doppler current profilers (ADCPs). While initially all three ADCPs were turned on, we relied primarily on the high-frequency TRDI WH300 that was best suited for the shallow research area. The data were collected with the University of Hawaii (UH) UHDAS software. Tuned over the years by UH staff, the software also applied automated data processing that generated a near-final data set. On roughly a daily basis, the complete processing directory ("proc") was transferred to a shore-based web site. At this point, additional quality control was done ashore, including further profile editing to address occasional noise during rougher sea states as well as removing a few remaining "sub-bottom" data that had made it past the automated UHDAS algorithms. Lastly, the Oregon State University tidal model (http://volkov.oce.orst.edu/tides; Padman & Erofeeva, 2004) was used to remove the barotropic tide. The accuracy of the velocity measurements is estimated to be 2 cm s^{-1} (Pickart et al., 2016).

Vertical sections of absolute geostrophic velocity were made by referencing the CTD-derived thermal wind shear using the ADCP velocity. In particular, we interpolated the cross-transect ADCP velocity onto the same grid as the CTD data, using NaNs in the near-surface and near-bottom blanking regions of the ADCP. Then, at each cross-stream grid point, we matched the vertically averaged ADCP velocity profile to the vertically averaged geostrophic profile over their common depth range to determine the reference velocity, then applied this to the geostrophic profile. Finally, we gridded the section of absolute geostrophic velocity at the same resolution as the CTD variables described above.

2.3. Historical Hydrography and Velocity

For part of the analysis, we utilize a historical data set of temperature and salinity profiles obtained from multiple data sources: (a) the Unified Database for Arctic and Subarctic Hydrography, for the period 1980–2015 (Behrendt et al., 2018); (b) the World Ocean Database 2018 (WOD18), obtained from the National Centers for Environmental Information, spanning 1894–2020; (c) a data set of hydrographic observations in the Chukchi Sea compiled by Danielson et al. (2020); and (d) shipboard measurements in recent years (up to 2020) from the Arctic Data Center that have not yet been incorporated into the data sets above.

In addition to the shipboard ADCP data from the 2023 *Sikuliaq* cruise, we use historical shipboard ADCP data from the recently compiled ChukSA climatology (Bahr et al., 2023). This product contains 95 ADCP data sets collected on the Chukchi shelf between 2002 and 2023, primarily obtained during the months of July to September. The velocity profiles were subject to rigorous editing and quality control, after which the barotropic tidal signal was removed using the Oregon State University tidal model (Padman & Erofeeva, 2004). For details the reader is referred to Pickart et al. (2023).

2.4. Sea Ice Imagery

Synthetic aperture radar (SAR) imagery was utilized from two satellite missions, RadarSat-2 (MDA Space) courtesy of the U.S. National Ice Center, and the RADARSAT Constellation Mission (RCM) operated by the Canadian Space Agency. These satellites are in sun-synchronous orbits and use active radar to scan the earth surface so they can generate images through clouds and at night. Their spatial resolution is typically 100 m/pixel —although it can be higher depending on the radar beam mode. During our cruise the coverage was typically once per day. Realtime data were accessed via a website in an unprojected sensor grid format. After download, the data were converted to a polar stereographic projection and pixel values scaled down from 16 to 8 bits using software developed from Open Geospatial Consortium (OGC) components.

Post cruise, the imagery was used to investigate the space/time variability of the ice edge. To do this, the daily composite sea ice images were georeferenced and then re-scaled to a consistent greyscale color axis. A 2-D Gaussian smoothing filter with a 30-pixel window was then used to enhance the contrast between open water and ice, and a contour was extracted that best represented the sea ice edge. The contour selection was performed iteratively: first, the 110, 130, and 150 greyscale values were extracted. Generally, the 110 or the 130 contours best captured the ice edge. However, in some cases these values were not suitable because the image was dark. For these darker images, the greyscale contour was lowered to 90 or 75, depending on the brightness of the image.

2.5. Ocean Reanalysis Fields

We use the GLORYS12v1 global ocean eddy-resolving reanalysis, distributed by the Copernicus Marine Environment Monitoring Service (CMEMS, https://doi.org/10.48670/moi-00021; Lellouche et al., 2021). It has a horizontal resolution of 1/12°, 50 vertical levels, daily time resolution, and is available from 1993 onward. It is based on the Nucleus for European Modeling of the Ocean (NEMO) model, with surface forcing from the ECMWF ERA-Interim reanalysis (1993–2018) and the ERA5 reanalysis (2019 onwards). GLORYS12v1 assimilates satellite observations of sea level anomaly, sea surface temperature, sea ice concentration, and vertical profiles of in situ temperature and salinity. Here, we use the temperature, salinity, and velocity fields.

2.6. Water Sample Data

Water samples were collected from the Niskin bottles for the measurement of maximum photochemical efficiency of photosystem II (Fv/Fm) to assess the photophysiological state of the phytoplankton. Fv/Fm was generally measured on samples collected near the surface (~ 2 m) and at the base of the mixed layer. Samples were measured using a Chelsea Technologies (Surrey, UK) LabSTAF fluorometer. In particular, 50 ml samples were collected directly from the Niskin bottles and placed in the dark at 2°C for a minimum of 30 min to allow all reaction centers to become open. Fluorescent light curves (FLC) were then carried out on each dark-adapted sample according to Schuback et al. (2021). The light protocol consisted of pulsing samples (100 or 200 μs) with a blue LED (452 nm) at an intensity that adjusted automatically based on the phytoplankton abundance (approximately 14,000–17,000 μmol photon m^{-2} s^{-1}). Each FLC included 8 actinic light levels (0–$\sim$1,000 μmol photon m^{-2} s^{-1}) which had a spectrum containing a peak at 455 nm and a shoulder from 480 to 655 nm. Fv/Fm was then determined from the 0 μmol photon m^{-2} s^{-1} actinic light level.

3. Results and Discussion

As noted in Section 2.1, the survey box was chosen so that its northern part was in concentrated pack ice, while the southern part was in open water. Even as the ice retreated northward during the 6-week study period, the box remained partially ice covered. During the final occupation, most of the box was in open water, and, what little ice remained, was less concentrated than earlier in the cruise (Figure 3). The wind conditions throughout the cruise were remarkably calm. The scalar-averaged wind speed in the study region for the period 15 June–31 July 2023 was 4.1 m s^{-1}. This is the weakest wind in the 44-year ERA5 record for this time of year on the northeast Chukchi shelf and is more than two standard deviations smaller than the climatological average.

3.1. Water Masses

The mean sections of hydrographic variables for the HR and HRE lines are shown in Figure 4, where the mean ice extent is indicated as well. At both locations, there is very cold, relatively salty water underneath the pack ice and warmer, fresher, more stratified water to the south—separated by a front. The transition from cold to warm occurs near the ice edge, although we emphasize that the front is not an ice edge front but rather a water mass front that extends throughout the water column. The fact that the ice edge coincided with the front was likely due to a combination of melting of the ice by the warm water and the fact that there was confluent flow directed toward the front (discussed below in Section 3.2). One should keep in mind that the winds were light, which meant that the dominant ice movement was due to advection by the flow field.

At this time of year there are both winter and summer water masses present on the northeast Chukchi shelf. We adopt a set of definitions for these water masses that have been used in numerous previous studies and are listed in Table 1. The two types of winter water are Newly Ventilated Winter Water (NVWW) and Remnant Winter Water (RWW). The former is water near the freezing point that was formed the previous winter via brine-driven
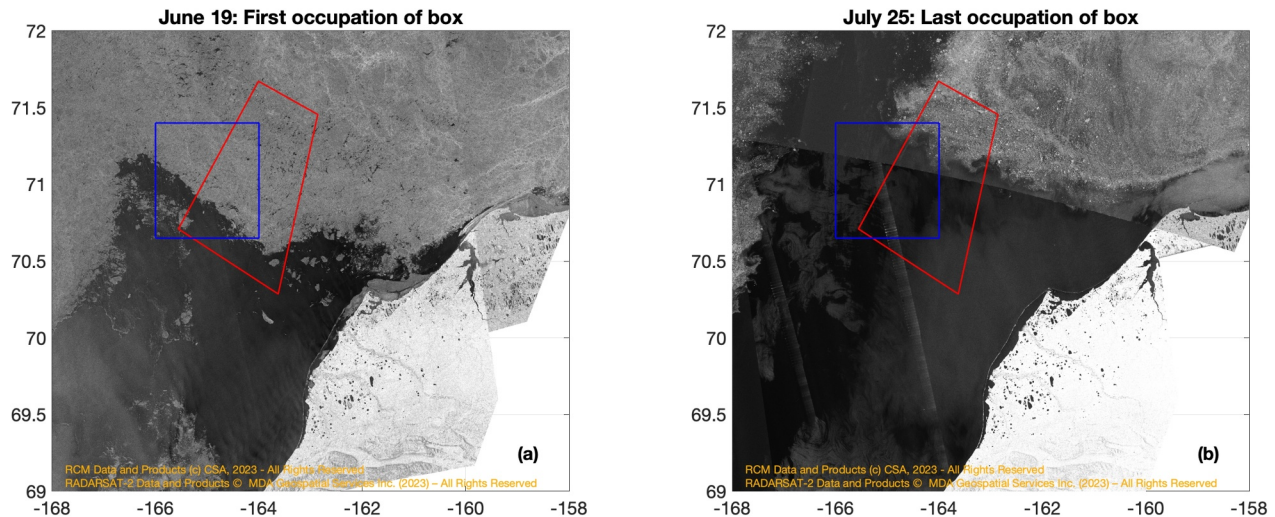
Figure 3. Synthetic aperture radar (SAR) images of the pack ice (a) shortly before the first occupation of the box (marked in red) and (b) shortly after the final occupation. The blue square is the domain used in Figure 14c for determining propagation of frontal meanders. See Section 2.4 for details of the SAR product and processing.

convective overturning as a result of ice formation (e.g., Pacini et al., 2019; Weingartner et al., 1998). The latter is moderated NVWW that has been warmed either by mixing with warmer surrounding water or via solar heating (Gong & Pickart, 2016). The two summer waters are Bering Summer Water (BSW), which is a mixture of Anadyr water and central Bering shelf water, and Alaskan Coastal Water (ACW) which stems from continental runoff. The final water mass is a combination of sea ice melt water and meteoric water, referred to as MWM; we assume that it is primarily melt water at this time of year in this location.

The volumetric temperature-salinity (*T-S*) diagram for the seven occupations of the box (Figure 5a) reveals that most of the water sampled was NVWW or water that had recently transitioned from NVWW to RWW (the precise division between the two is somewhat arbitrary). There was also a significant presence of BSW, along with smaller amounts of ACW and MWM. To show where these water masses resided in the vertical plane, we created what are referred to as water mass bin plots for the two lines (see, for example, Mastropole et al., 2017; Pacini et al., 2020; Pickart et al., 2023). Specifically, for each grid cell in the two sections we tabulated the number of realizations that a given water mass was present and expressed this as a percent between 0% and 100% (Figure 6). This shows that the majority of the water column (from 15 m to the bottom) beneath the ice was NVWW. This water mass contains the highest nitrate levels which spurred the phytoplankton bloom. On the southern side of the front, most of the warm water was a combination of BSW and ACW, with greater percentages of each on the HRE line. This is partly because, on the HR line, a sizable amount of melt water was found in the open water part of the section within the upper layer. By contrast, on the HRE line the melt water was more sporadic, with the largest percentage immediately adjacent to the ice edge. RWW resided predominantly in the upper layer beneath the ice and in the lower layer seaward of the ice.

To get a sense of the timing of the different water masses, for each grid cell in the T-S plane we documented the box # when the water was first sampled (Figure 5b). Most of the T-S range of the two winter waters was measured on the initial circuit, along with a narrower range of BSW. As time progressed, warmer RWW was sampled, along with a broader range of BSW. Most of the ACW was measured later in the cruise, from box #4 to box #7, with much of the warmest ACW not encountered until the final occupation of the box. Interestingly, different ranges of cold meltwater (<0°C) were sampled as we continued to occupy the box, while most of the warmest melt water (>2°C) was not sampled until the last three realizations of the box.

3.2. Circulation

The depth-mean flow vectors from the ChukSA ADCP climatology, averaged over the time period 2002–2023 (see Section 2.3), reveal the ACC flowing to the northeast toward Barrow Canyon (Figure 2). The Central Channel Branch pathway is also evident, part of which veers to the east and crosses the HR section. Another
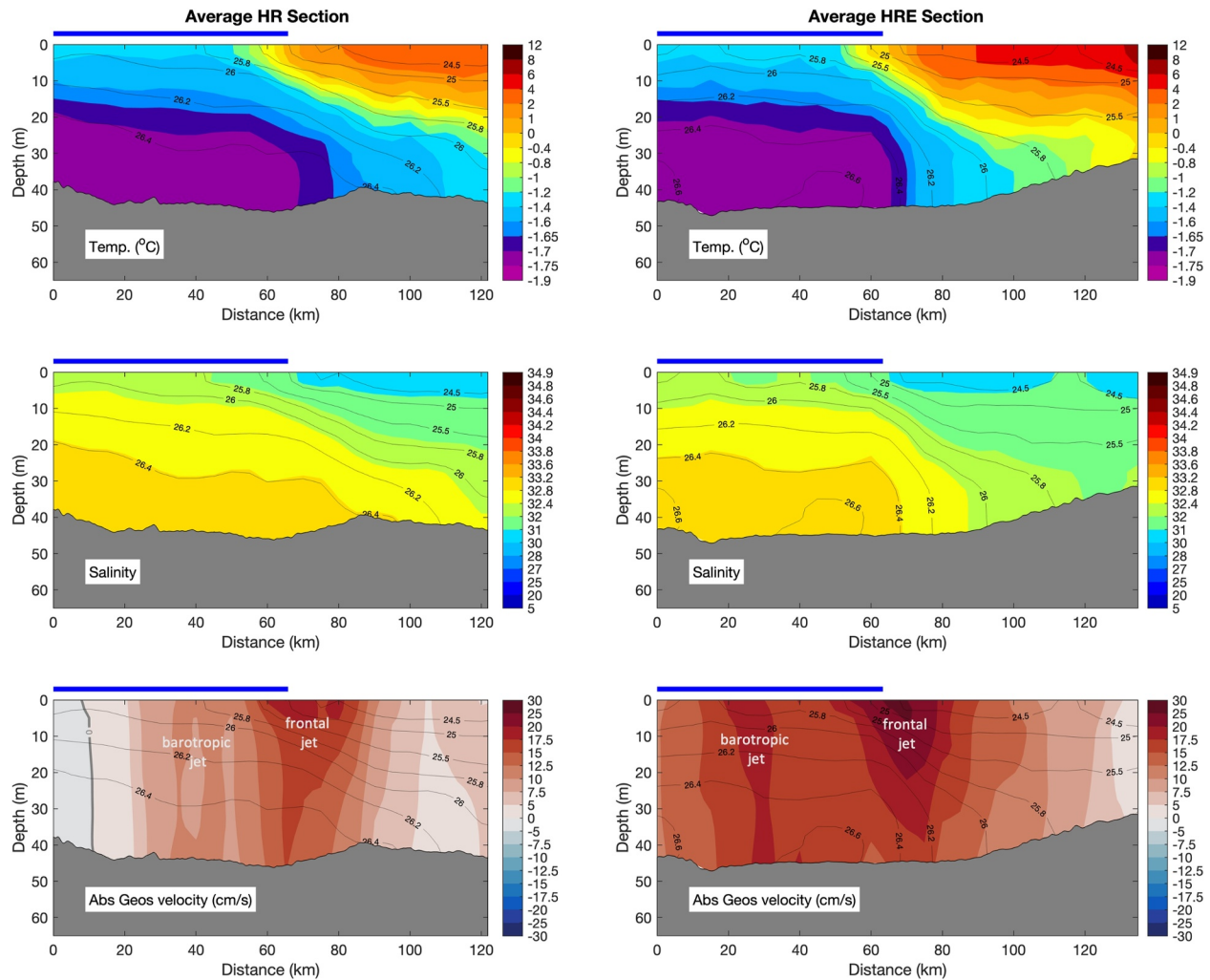
Figure 4. Mean vertical sections of temperature, salinity, and absolute geostrophic velocity for (left column) the HR line and (right column) the HRE line; the viewer is looking to the east. The contours are density (kg m^{-3}). The mean extent of the ice cover is indicated by the thick blue line. Positive velocities are to the east (the 0 cm s^{-1} contour is thick gray). The bottom is from Sikuliaq's echosounder. The two jets referred to in the text are labeled.

portion of the Central Channel Branch progresses farther to the north before retroflecting and flowing southward, crossing the northern side of the box. Finally, part of the Central Channel Branch flows anti-cyclonically around Hanna Shoal. These aspects of the flow on the northeast Chukchi shelf are well established via previous studies (e.g., Fang et al., 2020; Lin et al., 2019; Pacini et al., 2019; Pickart et al., 2016; Stabeno & McCabe, 2023; Tian et al., 2021; Weingartner et al., 2005). According to the ChukSA climatology, there is also flow into the box across its southern side, partly from the Central Channel Branch and partly from the ACC.

Table 1
Temperature-Salinity Definitions of the Water Masses Considered in the Study

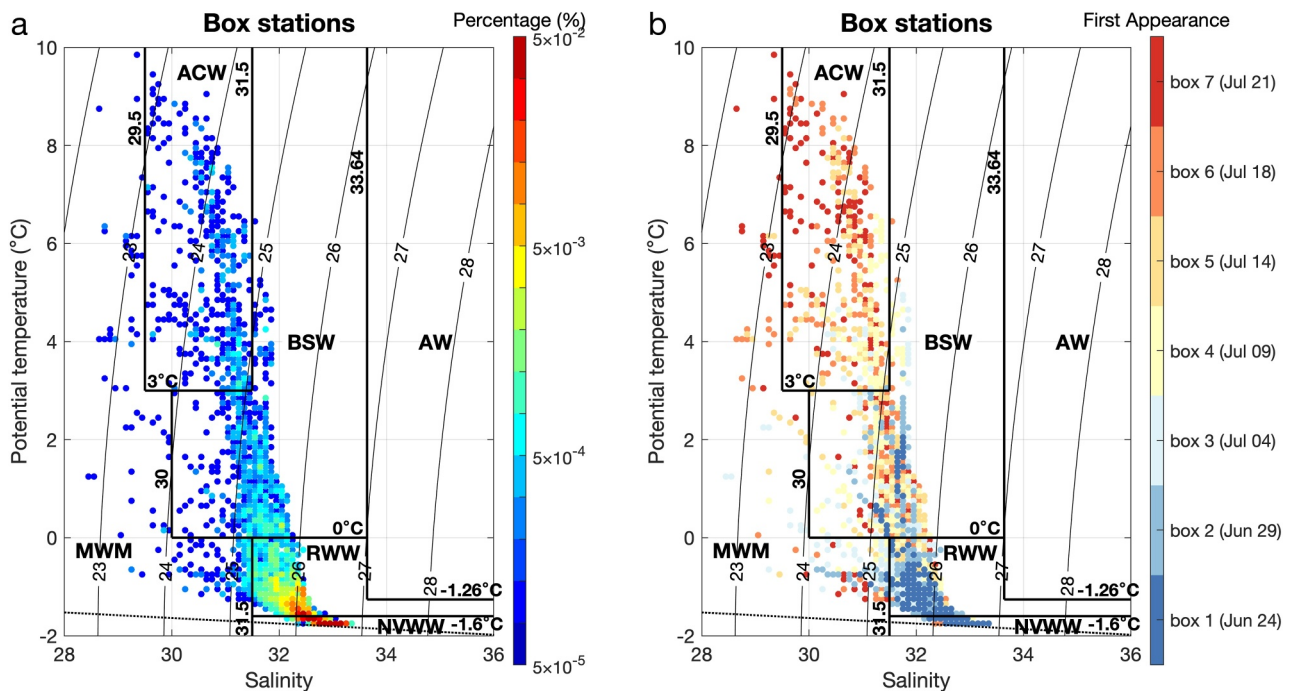|	
Alaskan Coastal Water (ACW)	$T > 3°C$, $S = 29.5–31.5$
Bering Summer Water (BSW)	$T = 0–3°C$, $S = 30–33.64$, and $T > 3°C$, $S = 31.5–33.64$
Remnant Winter Water (RWW)	$T = -1.6–0°C$, $S = 31.5–33.64$, and $T = -1.6--1.26$, $S > 33.64$
Newly Ventilated Winter Water (NVWW)	$T < -1.6°C$, $S > 31.5$
Melt Water/Meteoric Water (MWM)	$T < 0°C$, $S = 30–31.5$, $T < 3°C$ and $S = 29.5–30$, and $S < 29.5$

Figure 5. (a) T-S plot for the stations comprising all occupations of the box. The color denotes the percent occurrence for each bin of 0.1°C in temperature and 0.1 in salinity. (b Same as a) except the color denotes the box # when the water in the bin was first observed. The water mass acronyms are defined in Table 1 (we also include AW = Atlantic Water, although none was measured during the cruise).

In order to create the flow map in Figure 2, it was necessary to use the complete ChukSA data set from early summer to late fall (to get enough data coverage). Although our cruise only spanned mid-June to late-July, the velocity data from *Sikuliaq* are quite consistent with the mean ChukSA map (Figure 2). One sees that the flow is confluent: inflow across the western, northern, and southern sides, and stronger outflow across the eastern side. It is well established that the flow on this portion of the Chukchi shelf is sensitive to wind, and, under strong enough northerly winds, both the ACC and the Central Channel Branch reverse and flow toward Bering Strait (Lin et al., 2019; Pickart et al., 2011). However, as noted above, the winds throughout the study period were light, and no such flow reversals were observed.

Using *Sikuliaq's* ADCP data, we created sections of absolute geostrophic velocity (following the procedure in Section 2.2) along the four sides of the box for each occupation. Taking the mean of the seven occupations, we find that mass is balanced in the box within the uncertainty of the transport calculation (instrumental + statistical error). Remarkably, this is true for each individual circuit as well, attesting to the lack of wind forcing throughout the cruise. Taking positive transport as into the box and negative transport as out of the box, the mean transports for the four sides of the box are 0.17 ± 0.04 Sv (south), 0.48 ± 0.03 Sv (HR), 0.18 ± 0.03 Sv (north), and −0.83 ± 0.06 (HRE), which sum to zero. Despite the fact that some ACW was present toward the end of the cruise in the southern part of the HR and HRE lines, the ACC was not well-established in terms of velocity this early in the season. Notably, the mean transport of across the HRE line is very close to the mean transport of the Central Channel Branch determined by Pickart et al. (2023) using 17 years of data from the DBO3 line off of Pt. Hope (see Figure S1 in Supporting Information S1 for the location of the DBO3 line), 0.86 ± 0.11 Sv. This implies that our box captured most of the Central Channel Branch flow, perhaps missing a small amount that progresses around the north side of Hanna Shoal and drains into Barrow Canyon without reaching the top of the box (Figure 2).

The mean absolute geostrophic velocity sections of Figure 4 show that the density front on the HR and HRE lines supports a baroclinic jet flowing to the east. There is also a barotropic jet located under the pack ice. Both jets were present on both lines during each occupation of the box. We calculated the transport of each jet for each realization (Table 2). At the HR line the frontal jet on average has a larger transport than the barotropic jet, but the two jets have comparable transport at the HRE line. There is no obvious relationship with respect to the time variation of the jets over the course of the occupations.
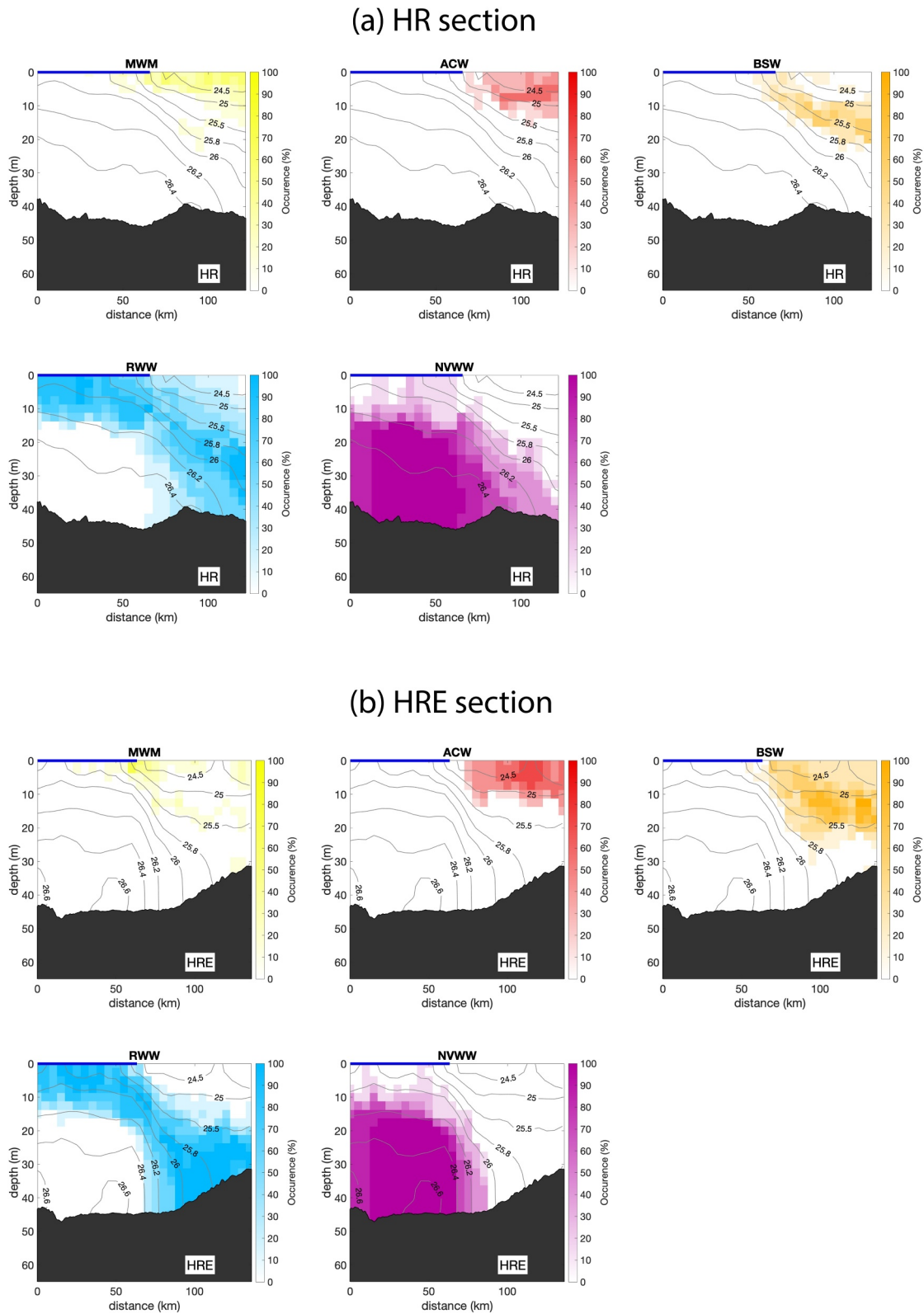
Figure 6. Water mass percentage occurrence at the (a) HR section and (b) HRE section. The mean extent of the ice cover is indicated by the thick blue line. See text for how the percentages were calculated. See Table 1 for the water mass acronyms. The bottom is from Sikuliaq's echosounder.

Table 2
Transports (in Sv) of the Frontal Jet and Barotropic Jet for Each Occupation of the HR and HRE Lines, Including the Mean Values

Hanna ridge			Hanna ridge east		
Section	Frontal jet	Barotropic jet	Section	Frontal jet	Barotropic jet
HR	0.23	0.15	HRE	0.24	0.25
HR2	0.18	0.20	HRE2	0.35	0.26
HR3	0.18	0.16	HRE3	0.40	0.40
HR4	0.18	0.20	HRE4	0.24	0.33
HR5	0.23	0.09	HRE5	0.23	0.27
HR6	0.16	0.07	HRE6	0.23	0.25
HR7	0.24	0.10	HRE7	0.31	0.25
Mean	0.20 ± 0.03	0.14 ± 0.05	Mean	0.29 ± 0.07	0.29 ± 0.05

Since the hydrographic front at the HR and HRE lines is not an ice edge front but rather a water mass front that extends throughout the water column, it is natural to wonder if the front and the two jets are present during the remainder of the summer. To address this we used the historical hydrographic data and ChukSA velocity data (Section 2.3). Considering the data from the open water period August to October, we identified a swath roughly coincident with the box and projected all of the profiles within the swath onto a line. The space-time data coverage for the hydrography and ADCP velocity are shown, respectively, in Figures S1 and S2 of Supporting Information S1, along with the stations used. Following this, we constructed vertical sections of the hydrographic properties and absolute geostrophic velocity (calculated the same way as for the *Sikuliaq* sections). This reveals that the front persists throughout the warm season and is not related to the presence of the ice (Figure 7). The difference later in the season is that the NVWW originally present on the cold side of the front is now replaced by RWW, and the water on the warm side of the front is now even warmer and fresher, dominated by ACW. The frontal jet is present in the historical mean section, as is the barotropic jet to the north.

The nature of the frontal jet and barotropic jet can be put into clearer context by comparing our sections to the mean DBO3 section farther south off of Pt. Hope from Pickart et al. (2023) (Figure S3 in Supporting Information S1). We note that the mean DBO3 section excludes time periods of southward flow reversals (see Pickart et al. (2023) for details), enabling a meaningful comparison to the *Sikuliaq* sections which were occupied under light winds. The DBO3 line is located south of where the Central Channel Branch begins to divide into different segments (see Figure S1 in Supporting Information S1). In the mean DBO3 section, which includes data from June to November, the Central Channel Branch is situated seaward of the ACC, with its offshore edge corresponding to the minimum in northward flow (see Pickart et al., 2023). One sees that the eastern part of the Central Channel Branch is more baroclinic, associated with a stronger frontal gradient, while its western part is more barotropic. Taken together with the results presented here, this indicates that the entire baroclinic part turns eastward after emerging from the Central Channel to flow through the box—roughly 70% through the western side, 30% through the southern side, and all of it crossing the eastern side. However, only about half of the barotropic part turns eastward at that point, with the remaining half flowing farther to the north and retroflecting back through the northern side of the box—all of it crossing the eastern side (except seemingly a small portion that progresses around the top of Hanna Shoal and then into Barrow Canyon). Note that, via this process, the barotropic part of the Central Channel Branch becomes separated from the baroclinic part, whereas the two are merged at the DBO3 line.

3.3. Growth and Sinking of the Phytoplankton Bloom

During the month-long period spent occupying the box, a phytoplankton bloom occurred predominantly under the ice. To characterize the evolution of the bloom, we chose the 4 mg m^{-3} fluorescence-based Chl *a* value as the bounding contour of the bloom for each section. Since the gradients at the edge of the bloom are large, the results below are not sensitive to this exact choice, as the resulting area hardly changes for other chosen values (see Figure S4 in Supporting Information S1 for an example showing the area bounded by the 4 mg m^{-3} contour offshore of the front). Next, we computed the average fluorescence value within this area, and also computed the mean vertical profile of fluorescence for all of the CTD stations within this region.

The time series of average fluorescence in the vertical plane nicely quantifies the growth and subsequent decay of the bloom along the two sides of the box (Figure 8, top panel). At each line the bloom approximately doubled in magnitude over roughly the first 2 weeks, then decayed by about half that amount over roughly the next 2 weeks. The average vertical profiles are displayed as a waterfall plot (Figure 8, bottom panel). For each profile we identified the depth of maximum fluorescence, then fit a regression line to this depth for the occupations when the bloom was near the surface and a second regression line for when the bloom was sinking. At both sides of the box the bloom stayed near the surface for roughly the first 2 weeks, then, as it began to decay, it sank at a rate that was remarkably consistent between the two lines, ~0.5 m/day. This value is similar to previous estimates of gravitational sinking (Bannon & Campbell, 2017; Eppley et al., 1967). We note that it could also reflect vertical
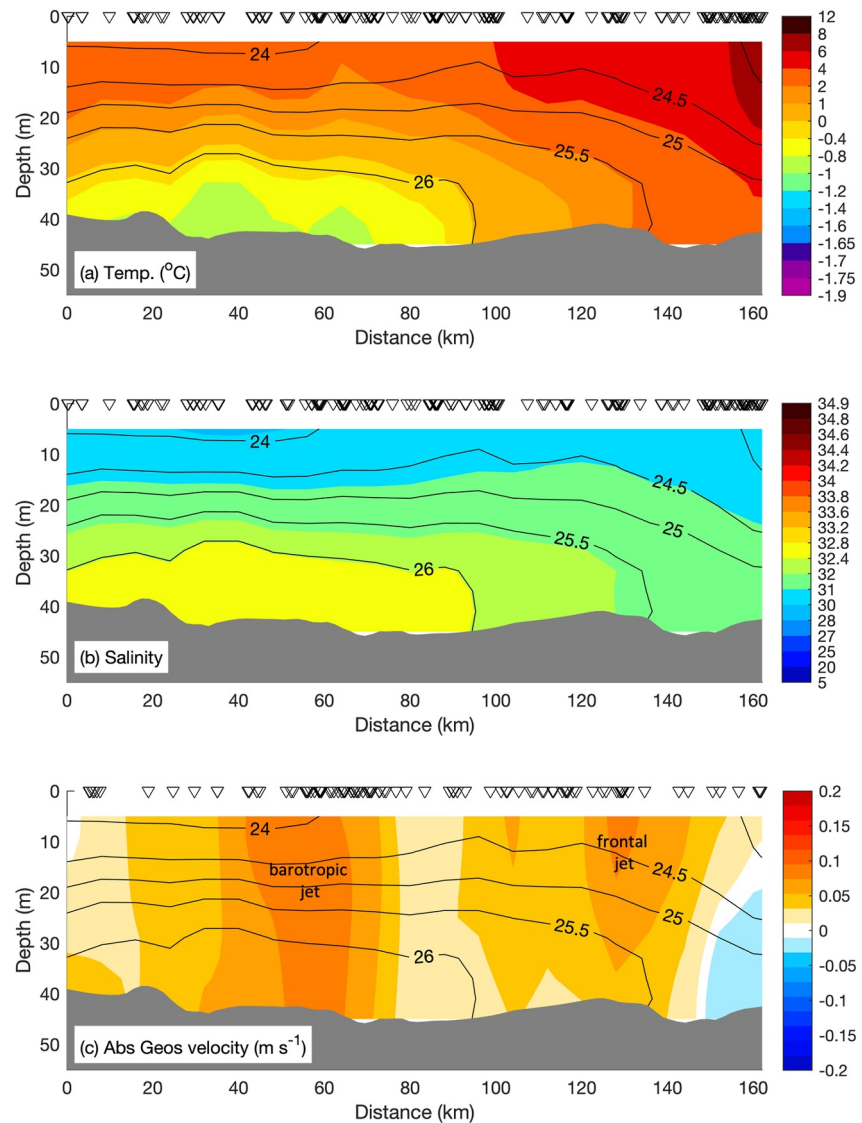
Figure 7. Mean vertical sections using historical data from August to October for the composite line roughly coincident with the box (see Figures S1 and S2 in Supporting Information S1). (a) Temperature; (b) salinity; (c) absolute geostrophic velocity (positive is eastward). The contours are density (kg m^{-3}). The locations of the projected stations are indicated along the top. The bottom depth is from ETOPO2. The viewer is looking to the east. The two jets referred to in the text are labeled.

migration of the phytoplankton to the nutricline. The typical euphotic depth during the study period was 20.4 ± 9.3 m.

Figure 9 shows the fluorescence sections for all of the HRE occupations (qualitatively these are similar to the HR line, Figure S4 in Supporting Information S1). On the initial occupation there was minimal bloom activity under the ice, but that changed quickly, and, from then on, nearly all of the phytoplankton growth was under the ice. As time progressed, higher levels of fluorescence were generally found farther within the ice pack (i.e., farther to the north). This is likely because more sunlight is able to pass through the thinner, less concentrated ice near the edge of the pack, which spurs earlier growth. Then, after the nitrate is drawn down there, the maximum growth shifted to where the NVWW—which contains the highest nitrate content—is closer to the surface, even though there is less sunlight farther into the ice pack. Ultimately, the bloom started to sink as the nitrate near the surface was drawn down (Figures 8 and 9). Perhaps the most striking aspect of these sections, however, is the plume of fluorescence that extends downward along the hydrographic front—along the isopycnals—in each of the occupations. This suggests that a ubiquitous process is pumping the phytoplankton to the sea floor considerably faster
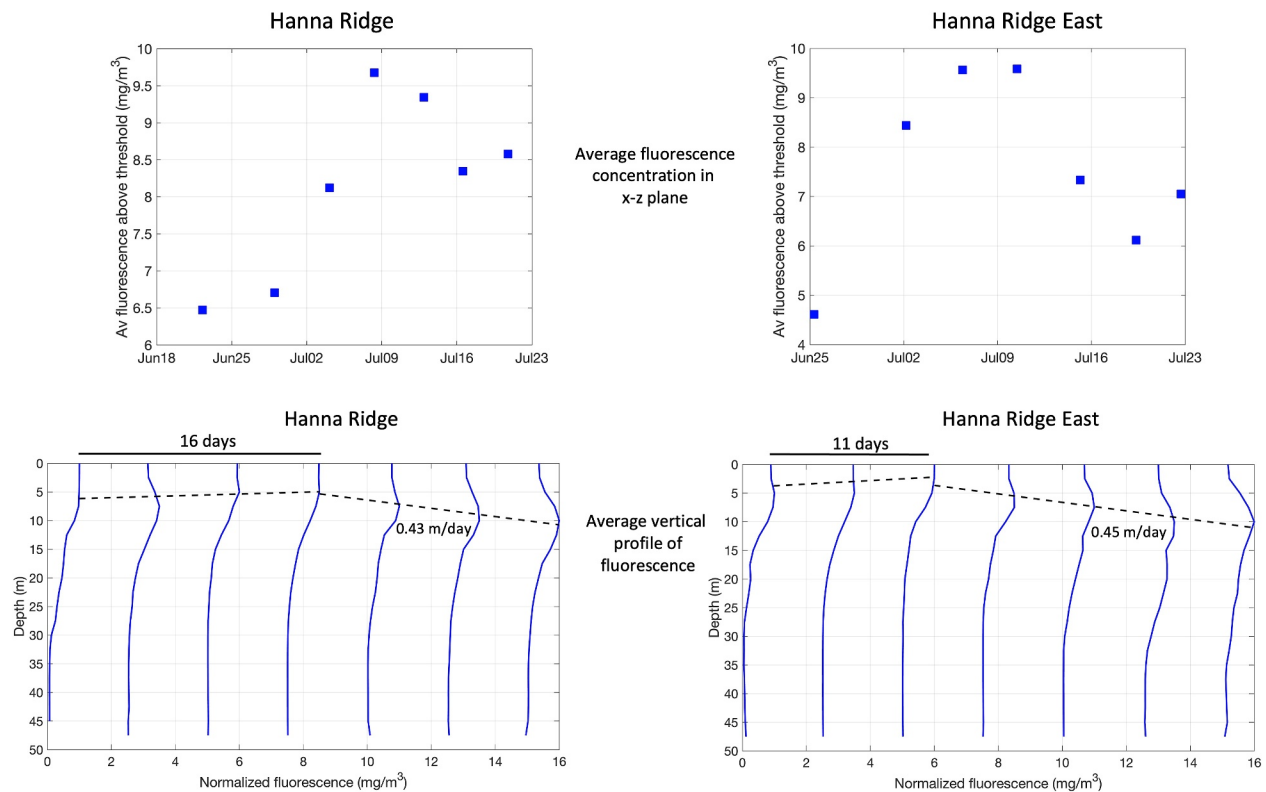
Figure 8. (top panel) Timeseries of average fluorescence of the phytoplankton bloom at the HR and HRE lines. The area of the bloom for each realization is taken to be where the fluorescence is >4 mg m^{-3} excluding the region of the hydrographic front (see text and Figure S4 in Supporting Information S1). Note that the y-axis range is different in the two plots. (bottom panel) Waterfall plot of the average vertical profile of fluorescence in the bloom for each successive occupation of the two lines. Each profile is normalized by its maximum value and offset by 2.5 mg m^{-3}. The dashed lines are the piecewise regression lines as explained in the text. The length of time the bloom remained near the surface is indicated along the top for each line.

than gravitational sinking. Note also that gravitational sinking would result in a more vertically oriented plume. We now explore this using a simple numerical model.

3.4. Frontal Dynamics and Enhanced Vertical Export

3.4.1. Numerical Model

An idealized, regional numerical model of a confluent frontal zone, motivated by the above observations, is now developed. The model is the MITgcm, which solves the primitive equations on a staggered C-grid in the horizontal and at constant depth surfaces in the vertical (Marshall et al., 1997). The model domain is 216 km in the along-front direction, 96 km in the cross-front direction, and $H = 50$ m deep with a flat bottom (Figure 10). The horizontal grid spacing is 500 m and the vertical grid spacing is 1 m. Horizontal viscosity is parameterized with the deformation-dependent Smagorinsky Laplacian operator with a nondimensional coefficient of 2.5 (Smagorinsky, 1963). Vertical diffusion of tracers is second order with coefficient 10^{-5} m^2 s^{-1} and vertical viscosity is second order with coefficient 10^{-4} m^2 s^{-1}. Density (ρ) is calculated from salinity (S) with a linear equation of state as $\rho = \rho_0 + \alpha_s(S - S_0)$, where α_S is the haline expansion coefficient and subscripts denote the basic state.

The model is initialized with a weak horizontal salinity gradient and a halocline in the vertical at 10 m depth (Figure 10). The salinity at the surface varies from 30.6 at the southern boundary to 32.25 at the northern boundary with a spatially uniform gradient in y. The horizontal salinity gradient is maximum at the surface and decreases with depth (Figure 10b), with a local maximum in stratification at 10 m depth. The stratification on the north side of the front is weaker than it is on the south side of the front. This initial state represents the juxtaposition of the NVWW to the north and the warmer, fresher BSW and ACW to the south. The velocity field is initialized such that it is in geostrophic balance with the density gradient provided by the salinity field.
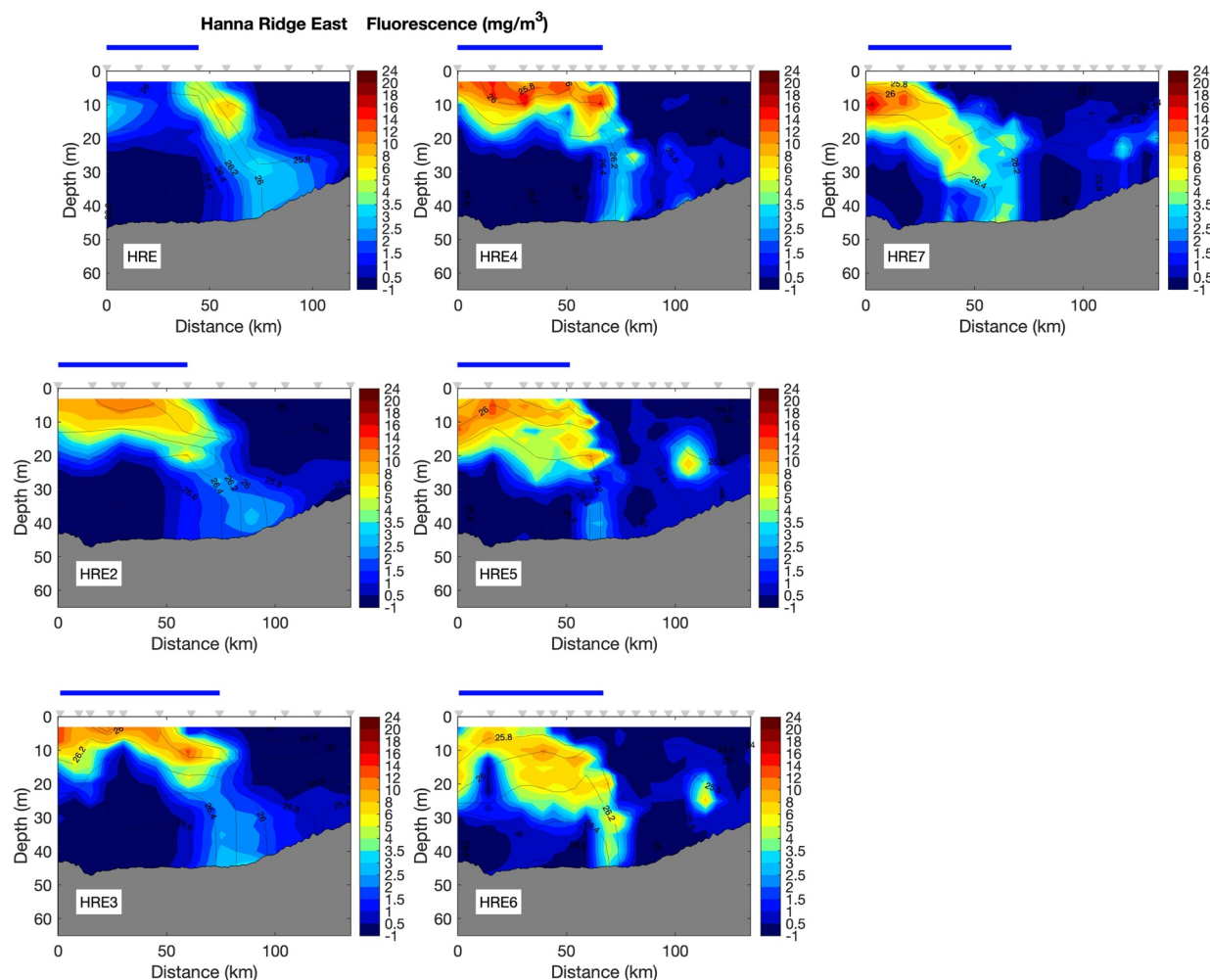
Figure 9. Vertical sections of fluorescence for the occupations of the HRE line. The contours are density (kg m^{-3}). The ice cover during each occupation is indicated by the thick blue line. The stations are listed along the top. The bottom is from Sikuliaq's echosounder.

The model also contains a depth-independent velocity component that is confluent, with southward flow through the northern boundary, northward flow through the southern boundary, and eastward flow through the eastern boundary. We note that this depth-independent component is not the barotropic jet described in the previous section; it is coincident with the baroclinic flow. The model does not contain the barotropic jet of the Central Channel flow branch. The western boundary in the model is closed. This depth-independent flow is specified through a transport streamfunction defined as $\psi = \gamma x (y - y_0)$, where $\gamma = 5 \times 10^{-5}$ m s^{-1} and $y_0 = 48$ km is the midpoint of the domain. This gives a depth-independent transport passing through the domain of 1 Sv. The bottom velocity is calculated from the streamfunction as $v = \nabla \times \psi / H$.

Recall that the bloom offshore of the front increased in magnitude for roughly 2 weeks, after which time it began to sink at ~0.5 m/day for roughly the next 2 weeks (Figure 8). A passive tracer is introduced in the model north of the front (defined by the 31.4 isohaline at the surface) that is set to a maximum value in the upper 13 m and decreases rapidly to zero with a vertical decay scale of 5 m. This represents the Chl a found in the near-surface bloom north of the front. The tracer "grows" from an initial value of zero to a maximum value of 1 at the end of the spin up period of 15 days. The tracer is advected and diffused in the interior in the same way as salinity and also grows at the same rate in the interior. The tracer is also advected in through the northern boundary. After the tracer reaches its peak, it is then forced to sink at a prescribed rate.

The initial state described above does not represent the sharp front observed, especially along the eastern line. Rather than define a narrow frontal region in the initial state, we allow the depth-independent confluent flow to
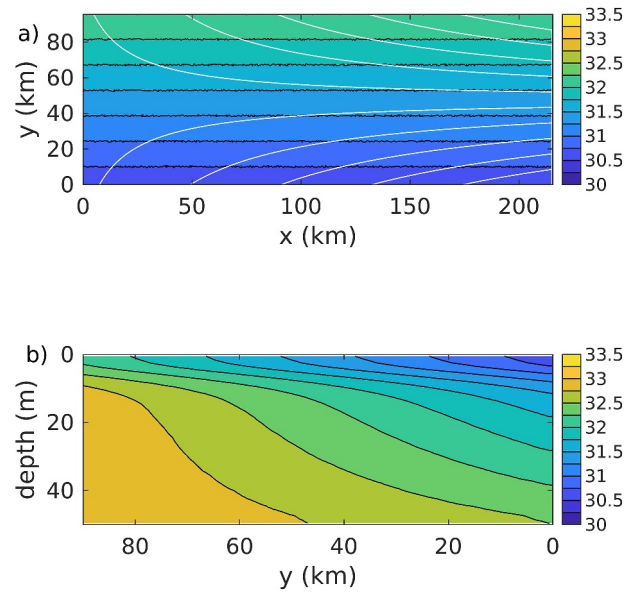
Figure 10. Model domain and initial conditions. (a) Sea surface salinity (colors) and barotropic streamfunction (white contours, contour interval 0.1 Sv). (b) Vertical section of salinity.

develop a frontal zone based on the water masses supplied at the northern and southern boundaries and the strength of the flow. Such a confluent flow not only develops a sharp front but also continually supplies potential energy to the domain that can maintain a baroclinically unstable flow for long time periods—which is not possible with an initial baroclinic front in a periodic channel (Spall, 1997). After the 15-day spin up period the front has sharpened and has started to become baroclinically unstable (Figure 11a). This state is taken to be day 0 of the simulation. The tracer no longer grows but is still advected into the domain through the northern boundary. After 11 additional days, the frontal region has further sharpened and developed strong meanders all along the front (Figure 11b).
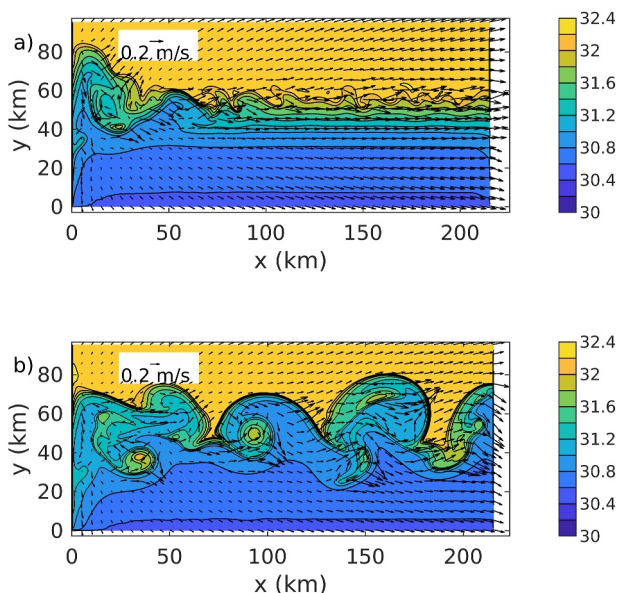

Figure 11. Sea surface salinity and horizontal velocity (every 10th grid point) at (a) day 0 and (b) day 11 of the simulation.

Three different tracer scenarios are considered. In the first case, the sinking rate is set to zero so that the source of tracer at the northern boundary remains concentrated near the surface and the tracer is moved only by advection and diffusion. This is referred to as the eddy case, since the vertical advection arises from the turbulent motions associated with the baroclinic instability of the frontal jet. In the second scenario, in addition to being advected and diffused, the tracer is specified to sink at the rate of 0.5 m/day in both the interior and along the northern boundary. This is called the eddy + sinking case. In the third scenario, the tracer distribution after spin up simply sinks at 0.5 m/day at each horizontal location with no advection or diffusion. This is called the sinking case. These three scenarios, which are run for 2 weeks, allow us to infer the relative importance of the ocean circulation, particle sinking, and their combination on the subduction of *Chl a* in the frontal zone.

For the case with eddies and 0.5 m day^{-1} sinking, the tracer extends close to the bottom in the frontal zone over the 2-week period. This is evident from the horizontal tracer distribution on day 11 at 40 m depth (Figure 12a). The tracer value at that depth is very small everywhere away from the front. However, under the front there is a swath of enhanced tracer values approaching 1, indicating that those waters have been brought down from the upper ocean relatively quickly and with very little mixing. The regions of tracer subduction lie below the surface signature of the frontal meanders (compare with Figure 11b).
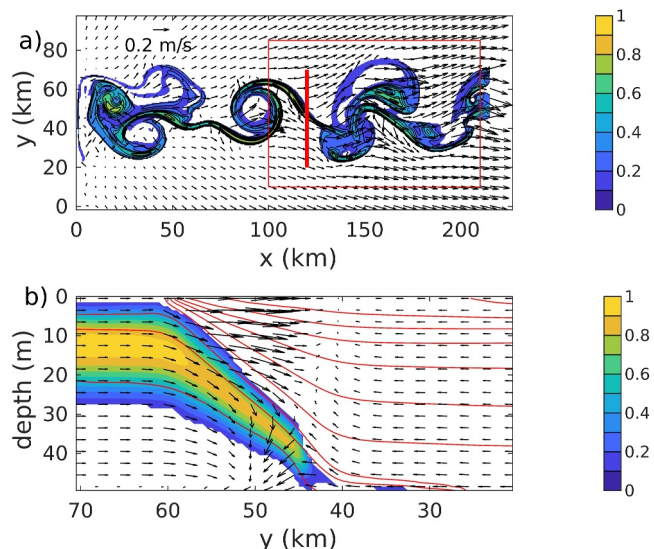
Figure 12. (a) Passive tracer at 40 m depth on day 11 for the eddy + sinking case (0.5 m day^{-1} sinking). (b) Vertical section along the thick red line in (a) of the passive tracer (color), velocity in the y–z plane (vectors), and isohalines (red lines, contour interval 0.25). The red box in (a) is the averaging area used to calculate the vertical fluxes in Figure 13. Areas where the tracer is less than 0.1 are white.

The pathway by which the tracer is transferred to depth is indicated by the vertical section across the front shown in Figure 12b. North of the front, the core of the tracer is situated between 10 and 15 m depth. This reflects the initial maximum located in the upper 10 m and a sinking rate of 0.5 m/day acting over 11 days. However, at the front, the tracer penetrates close to the bottom. This represents an effective vertical velocity of over 4 m/day or roughly an order of magnitude greater than the sinking rate. The path of the subducted tracer lies along a sloping isopycnal, indicating that this is driven by advection and not vertical mixing. The cross-stream and vertical velocity shows strong vertical transports in the frontal region. Away from the front, there is the confluent flow with weak upwelling on the fresh (anticyclonic) side of the front and weak downwelling on the salty (cyclonic) side of the front. (The velocity vectors do not align exactly with the isohalines because the flow is not steady.)

The effectiveness of this eddy-driven vertical transport in the frontal region is measured by the vertical flux of tracer integrated over the region marked by the red box in Figure 12a over the 2-week integration time after the tracer was fully grown and began to sink. We scale this by the total horizontal flux through the northern boundary of the box. Near the surface, where the vertical velocity is small, the fraction of tracer flowing into the basin that gets pumped downward is small. However, for the model run with both frontal instabilities and a background sinking rate of 0.5 m/day (eddy + sinking), about 30% of the tracer fluxed into the box is pumped downward below 20 m depth (Figure 13). For the case with no currents and only an imposed sinking (sinking only), only about one third of that amount sinks below 20 m and the maximum downward transport of 15% is found shallower in the water column. No tracer penetrates below 30 m depth in this case simply because the model has not been integrated long enough. The case with the unstable front and no background sinking (eddy only) also produces less downward transport than the first scenario with a maximum of less than 20% below 20 m depth.

We note that the vertical transport of tracer below 20 m for the case of eddy fluxes plus sinking is larger than the sum of the other two cases. The reason for this is that the vertical profile of the eddy fluxes has a first baroclinic mode structure, which means its horizontal velocity is largest at the surface while its vertical velocity is largest at mid-depth, just below the halocline. The key role that the sinking plays in getting more tracer to depth is by allowing it to sink away from the surface, where the eddy vertical velocities are weak, to the halocline depth, where the eddy vertical velocities are large. However, the first baroclinic mode structure also means that the eddy vertical velocities are small near the bottom, thus the frontal instability process is unable to help transport the tracer all the way to the seafloor. It is likely that vertical motions in the bottom boundary layer (BBL) accomplish this. We computed the BBL height at each CTD station following the methodology of Pickart et al. (2002). During the occupations of the box there was a weakly stratified BBL which on average was 11.0 ± 4.6 m thick and corresponded to a region of low beam transmission. This means that the subduction mechanism need only bring the Chl a to roughly 10 m above the bottom, at which point BBL processes should deliver it to the sediments.

3.4.2. Inferences From the Data

3.4.2.1. Phytoplankton Response

The numerical model results suggest that, in the vicinity of the front, Chl a is pumped downward at >4m/day. For a starting depth of 10 m and a bottom depth between 40 and 45 m, this means that the Chl a should reach the BBL (order 10 m thick) in 5–6 days. To put this in perspective, the average speed of the frontal jet is roughly 15 km/day, which means that the advective time
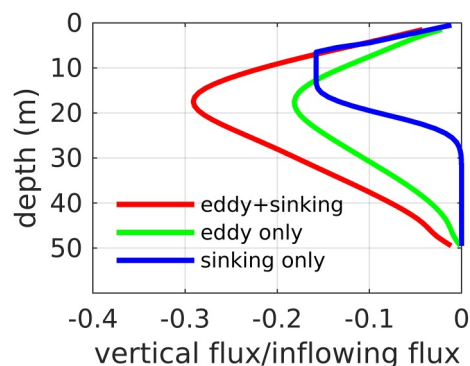

Figure 13. Vertical flux of tracer integrated over the red box in Figure 12a and averaged in time for the 2-week integration after the spin-up. Red line: active eddy fluxes and an imposed sinking rate of 0.5 m/day. Green line: eddy fluxes only. Blue line: sinking only. Fluxes are scaled by the total horizontal flux of tracer through the northern boundary of the box.

between the HR and HRE lines is approximately 5 days. Hence, Chl a within the under-ice bloom at the HR line should be pumped to the BBL by the time it reaches the HRE line. Such rapid export in turn implies that the phytoplankton within the plume should still be relatively healthy. This can be assessed by analyzing the ratio Fv/Fm of the ambient phytoplankton community (see Section 2.6).

Fv/Fm was mainly collected on samples in the top 15–20 m of the water column. We identified all of the samples within the bloom north of the front for each realization (using the same 4 mg m^{-1} criterion to define the bounds of the bloom, see Figure S4 in Supporting Information S1). The average Fv/Fm along the HR line was 0.55 ± 0.020, and that for the HRE line was 0.59 ± 0.015. This indicates that the phytoplankton were photosynthetically active throughout the measurement period (Gorbunov & Falkowski, 2022). The timeseries of Fv/Fm within the bloom shows no trend at HR and a slight (but statistically significant, $P = 0.005$ and $R = 0.940$) negative trend at HRE (Figure S5 in Supporting Information S1).

In an effort to explain some of the observed scatter in Fv/Fm, we considered the photosynthetically active radiation (PAR) data from the sensor mounted on *Sikuliaq's* main mast at a height 14.3 m above the water line as well as from the sensor on the CTD package. A clear diurnal cycle was present in the mast data as well as in the top 5 m of the water column; the amplitude of the CTD signal was about half that of the signal in air. Previous studies have documented a diurnal cycle in Fv/Fm that is out of phase with that of the near-surface PAR (Schuback et al., 2016). We see no such relationship in our bloom data: the Fv/Fm signal is relatively constant throughout the day-night cycle. We also compared our Fv/Fm data with the bottle nitrate data as well as with the CTD fluorescence data. In both cases, there were slight correlations that were statistically significant (P values of 0.035, 0.002 and R values of 0.370, 0.554 for nitrate and fluorescence, respectively). In particular, the value of Fv/Fm tends to be higher when the nitrate content of the water is greater and when the fluorescence is higher. While both of these trends are expected, this does not quantitatively account for the observed scatter in Fv/Fm within the bloom seen in Figure S5 of Supporting Information S1. We hasten to add, however, that the observed scatter is in fact quite small, with an overall standard deviation of 0.02 compared to the overall mean of 0.55.

There are much less Fv/Fm data deeper in the water column. On the occupations of the HR line, there were only a total of five samples taken within the fluorescence plume along the front, and for the occupations of the HRE line there were only six. While this is obviously a small number of data points, a clear message nonetheless emerges. At both lines, the values of Fv/Fm in the plume are systematically lower than those typically found in the near-surface bloom (Figure S5 in Supporting Information S1). However, the plume values are still relatively high, indicating that phytoplankton transported to depth by the frontal secondary circulation were still fully capable of photosynthetic activity in relation to when they were near the surface. This supports the model conclusion that the frontal pumping mechanism is rapid.

3.4.2.2. Meander Scales

As discussed earlier, the location of the ice edge tracked that of the front throughout the study period (Figure 9). Since the sea ice edge was often corrugated in a regular pattern (see the 25 July image in Figure 3b) and the wind was very light for most of the cruise, we assume that these patterns were a reflection of the meandering water mass front. This motivated us to use the ice imagery to characterize the meander scales and compare them to those present in the model.

For each day, the meanders along the ice edge were defined through visual inspection (using the digitized ice edge contour defined in Section 2.4) and manually selected. This was done by comparing the ice edge contour and the associated ice image, to ensure that the meanders along the contour coincided with meanders in the ice edge itself, and not with detached ice floes near the ice edge or artificial fronts introduced when two satellite passes, with different brightness, were patched together. The peaks and troughs of the meanders were identified and the distance between these points was computed, providing a wavelength estimate for each meander. Following this, we computed the peak-to-trough amplitude of each meander, roughly perpendicular to the ice edge. During the study period, both isolated features and wave trains were present, with most of the meanders being part of wave trains. We note that there was some uncertainty in the exact location of a peak or trough, since not all meanders exhibited perfect sinusoidal behavior. To account for this uncertainty, all wavelengths were binned into 5 km intervals.
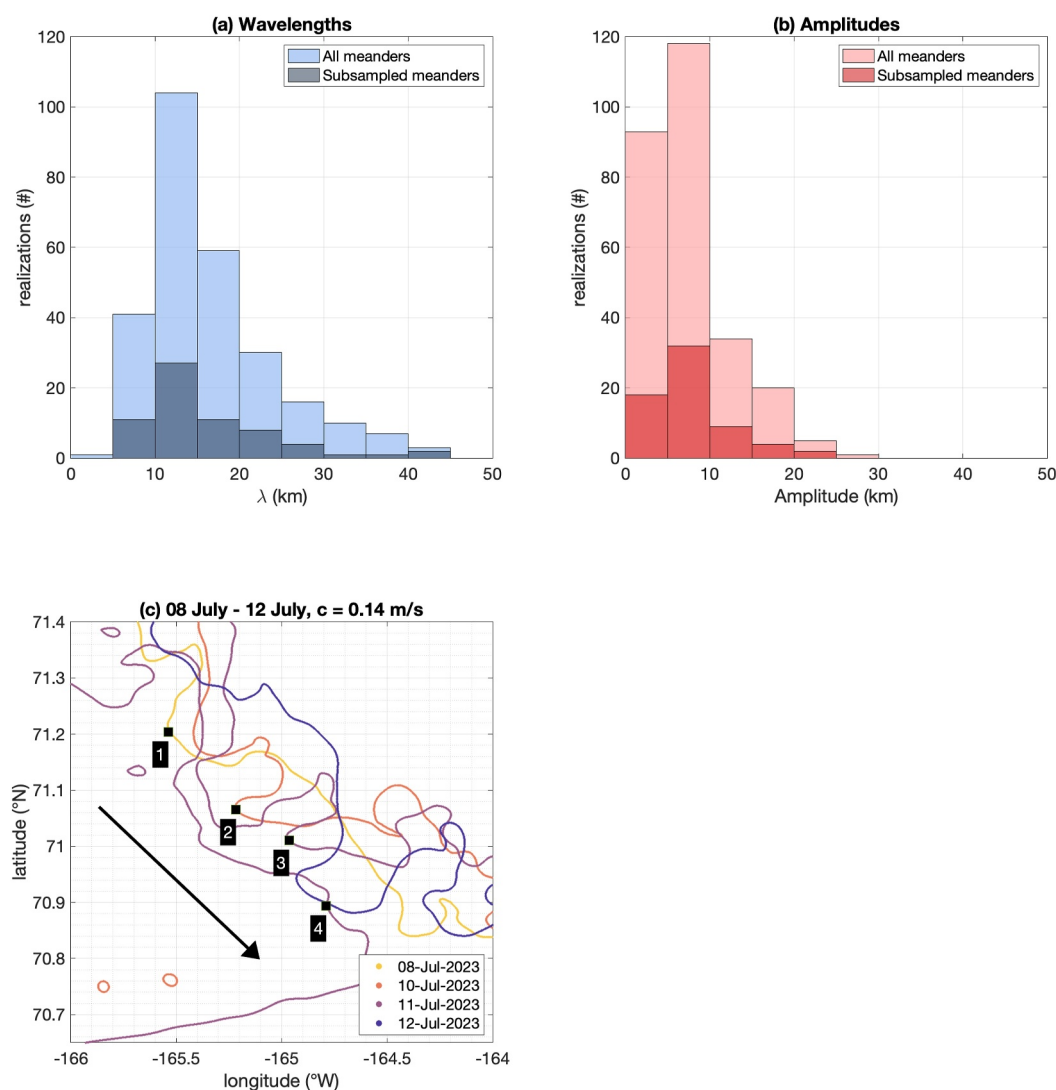
Figure 14. Histogram of (a) meander wavelengths and (b) meander amplitudes computed using the digitized ice imagery for all of the identified features (light color) and the independent realizations (dark color). (c) Contours of the ice edge from 8 to 12 July used to estimate the meander propagation speed. The numbered squares denote the meander peak locations used for the calculation. The geographical domain is indicated by the blue box in Figure 2.

The resulting distribution of all wavelengths shows a clear peak at wavelengths of 10–15 km and a long tail extending to meanders as large as 40 km (Figure 14a, light color). The amplitudes are generally smaller than the wavelengths, with most meanders exhibiting amplitudes between 5 and 10 km (Figure 14b, light color). We note that, in these histograms, some meanders are double-counted as they persist from 1 day to the next. However, the meander pattern was occasionally absent in an image. This was likely the result of a wind event and/or a melt-back event. Following such events, the meanders would again develop. Approximately every 7–10 days an ice edge without meanders was observed. Hence, in order to compare independent realizations, the same histogram was re-computed using a subset of images spaced on average 5 days apart over the 42-day record. While this resulted in reduced statistics, the same general pattern was found, with wavelengths of 10–15 km (Figure 14a, dark color) and amplitudes of 5–10 km (Figure 14b, dark color) being the most prominent scales.

The next question is, do these features propagate, and, if so, can we quantify the propagation speed? To answer this, the ice edge was scrutinized over consecutive 5-day intervals which revealed clear instances of wave propagation. Using feature-tracking of the crests and troughs between successive ice images, we estimated propagation speeds for three especially clear instances of propagation: 25–28 June, 4–7 July, and 8–12 July. The
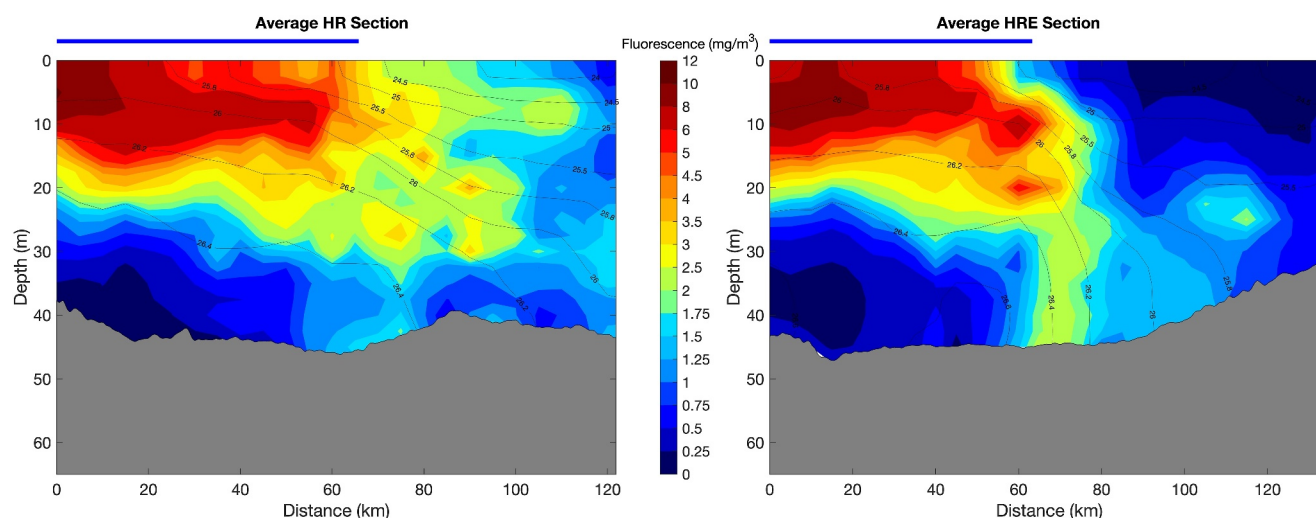
Figure 15. Mean vertical sections of fluorescence (color) and potential density (kg m^{-3}) for the (left) HR and (right) HRE lines. The mean ice cover is indicated by the thick blue line. The bottom is from Sikuliaq's echosounder.

last scenario is shown in Figure 14c. These three realizations exhibited average propagation speeds of 17, 15, and 14 cm s^{-1}, respectively.

To compute the analogous meander scales for the model, we defined the front by an isohaline and plotted it once per day. Wavelengths and amplitudes were estimated when a meander was clearly identified, and propagation speeds were calculated using similar feature tracking as was applied to the ice images. The model wavelengths so calculated increased as the simulation progressed in time (see Figure 11), which could be the result of turbulent cascade or longer waves having a slower growth rate. Overall, the model results were encouragingly similar to the observationally derived scales: wavelengths on the order of 20 km (10–15 km for the observations), amplitudes on the order of 15 km (5–10 km for the observations), and propagation speeds on the order of 10 cm s^{-1} (14–17 cm s^{-1} for the observations).

3.5. Implications for the Sediments

3.5.1. Vicinity of the Box

The results presented above demonstrate that phytoplankton are preferentially and rapidly fluxed downward due to baroclinic instability of the frontal jet associated with the Central Channel flow branch. The obvious next question is, does this significantly impact the delivery of Chl *a* to the sediments? Figure 15 compares the mean density and fluorescence sections at HR versus those at HRE. On the western line (HR), the hydrographic front is fairly broad, and, while there is clearly a corresponding fluorescence plume directed along the front, the concentrations are not especially high near the bottom. By contrast, on the eastern line (HRE) the front is much sharper—due to the confluent flow—and higher levels of fluorescence extend to the bottom. The chlorophyll sediment data collected during the occupations of the box are consistent with the sections of Figure 15 (Lauer et al., 2024). In particular, higher levels of sediment Chl *a* were measured where the plume of fluorescence reaches the bottom on the HRE line (36.4 ± 8.6 between 60 and 120 km), while the sediment Chl *a* levels were uniformly moderate along the HR line (14.4 ± 2.3).

One should keep in mind that these comparisons apply to the mean conditions. As noted above, the individual realizations of the HR line showed plumes of high fluorescence extending to the bottom (Figure S4 in Supporting Information S1). The difference with this line compared to HRE is that the location where the plume reached the bottom on the individual HR realizations spanned a large distance across the section. This is highlighted by computing the fluorescence anomaly for each occupation relative to the mean section (Figure 16). The near-bottom region of high positive anomaly progresses from the southern end of the section, during the early occupations, to the middle of the section by the final occupation. This is partly due to movement of the deep part of the front but also due to the sinking of the near-surface part of the bloom north of the front quantified above
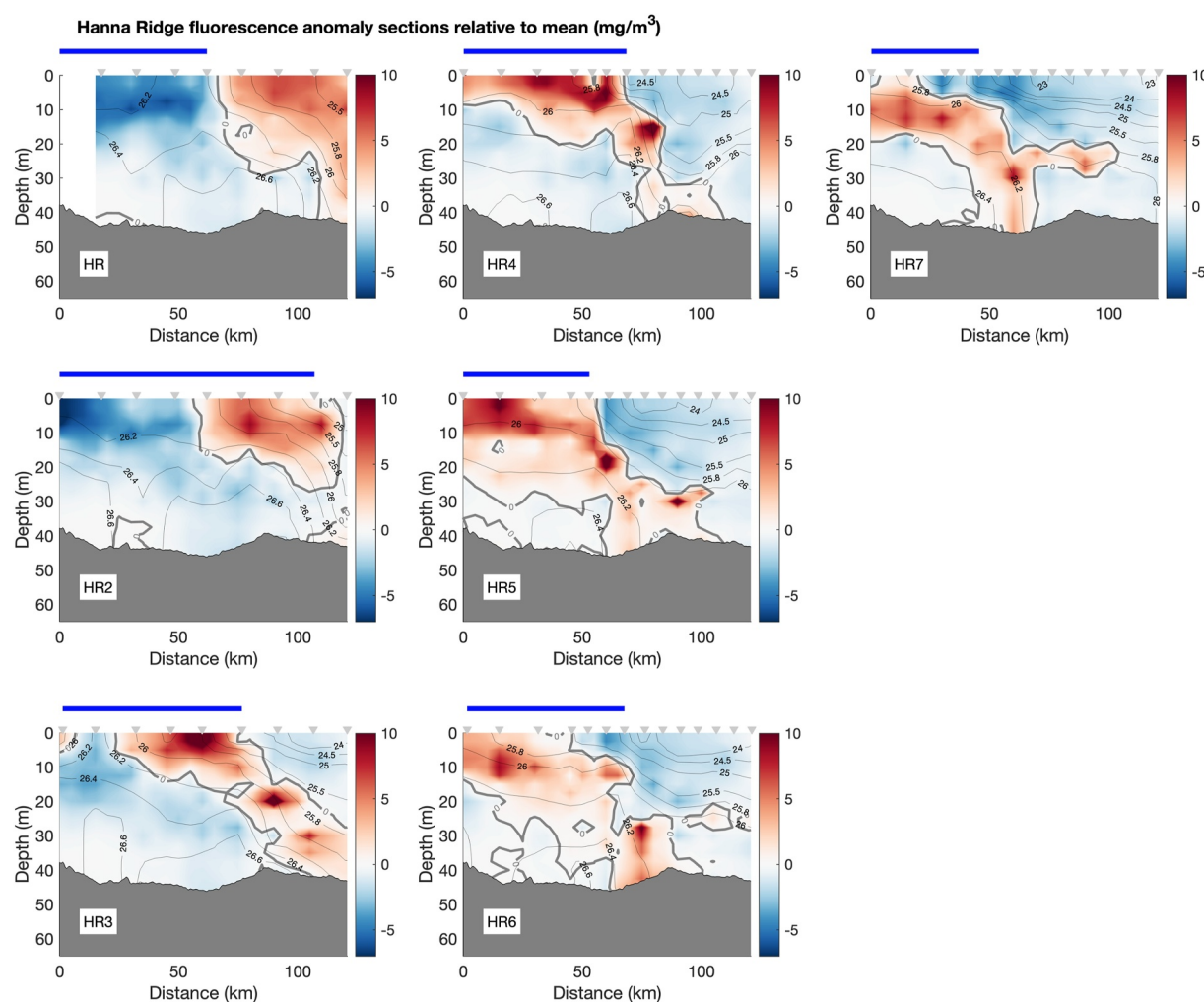
Figure 16. Vertical sections of fluorescence anomaly (from the mean) for the occupations of the HR line. The contours are potential density (kg m^{-3}) for each section. The ice cover during each occupation is indicated by the thick blue line. The stations are listed along the top. The bottom is from Sikuliaq's echosounder.

(Figure 8). The anomaly sections show especially clearly how initially there was some bloom activity in open water (although some loose ice was present in the vicinity), then a pronounced bloom under the pack ice which eventually began to sink. From HR4 to HR7 the sinking Chl a under the ice progressively reached deeper isopycnals, which in turn grounded farther toward the offshore edge of the front—that is, at a more northern location. By contrast, the front at HRE grounded more consistently near the same location, and the front was sharper (less lateral separation between isopycnals), both of which led to a more focused region where the Chl a reached the bottom.

3.5.2. Broader Context

It should be kept in mind that the part of the bloom north of the front is sinking due to gravity and that some portion of it eventually reaches the bottom (Lalande et al., 2020). Hence, one wonders if, at the end of the season, the frontal pumping matters for the total supply of carbon to the northeast Chukchi shelf. On the other hand, one could also envision that the sinking rate is slow enough that a significant portion of the bloom north of the front is advected off the shelf prior to reaching the bottom. We now address this using the GLORYS12v1 ocean reanalysis product.

We analyzed the GLORYS12v1 horizontal velocity and hydrographic fields for several summers—the results presented here for 2023 are representative of other years as well. The depth-mean velocity for July–August 2023 shows the expected circulation pattern on the northeast Chukchi shelf (Figure 17a). In particular, the Central
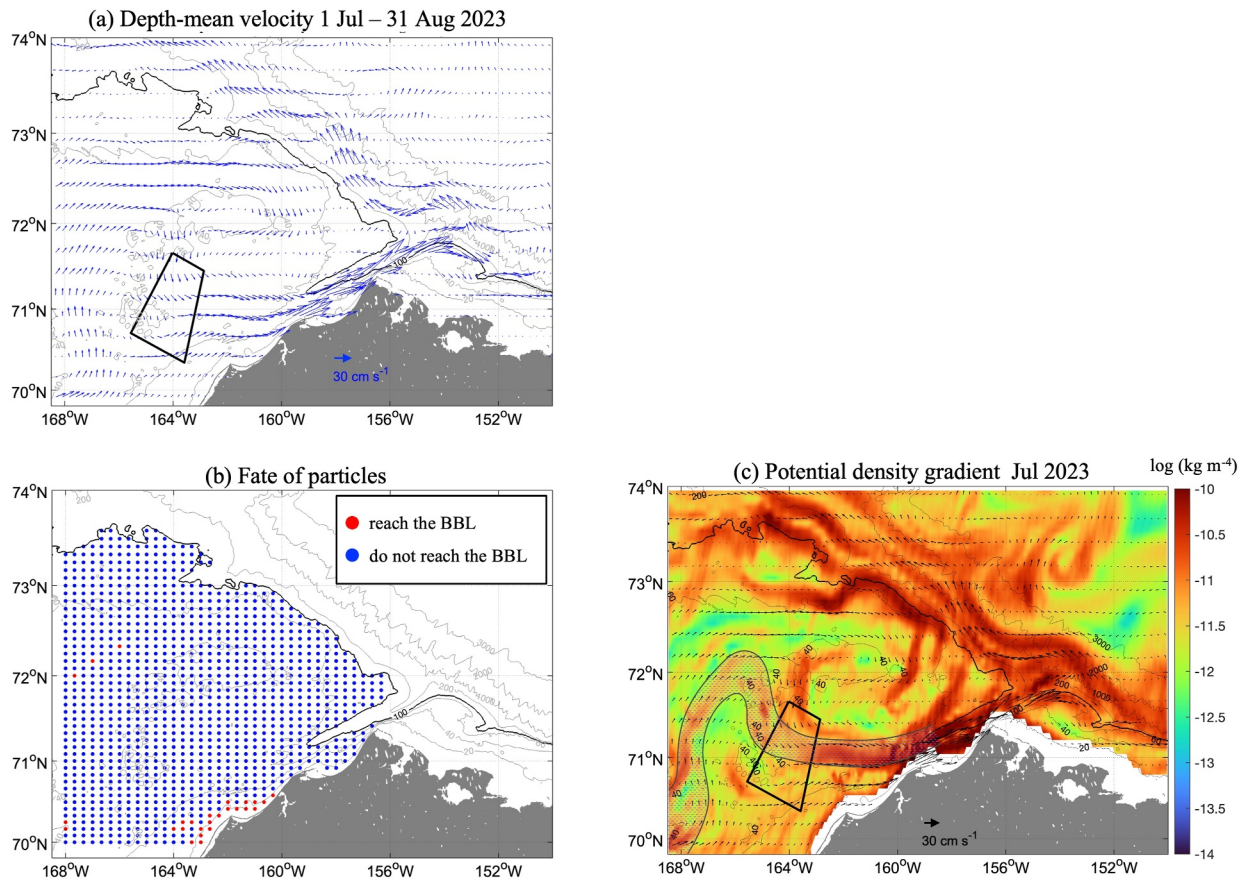
Figure 17. (a) Depth-mean vectors for July–August 2023 from GLORYS12v1. The box occupied during the *Sikuliaq* cruise is marked. The bottom depth is from ETOPO2, and the 100 m isobath is highlighted. (b) Locations where the particles were released on 1 July. The particles that reached the bottom boundary layer (BBL) before exiting the shelf are colored red, and those that exited the shelf prior to reaching the BBL are colored blue. (c) Mean lateral density gradient at 11 m depth for July 2023 from the GLORYS12v1 reanalysis fields. The velocity vectors at 11 m are overlaid. The region of enhanced density gradient associated with the Central Channel flow branch is hatched.

Channel flow branch splits in the same way that is seen in the ChukSA depth-mean velocity map (compare Figures 2 and 17a), and there is confluent flow into the box that was occupied during the *Sikuliaq* cruise. To address the fate of the sinking Chl *a*, we released particles on Jul 1 at every grid point on the shelf at a depth of 10 m (Figure 17b), which were advected according to the daily evolving flow field. We considered the entire region to the shelfbreak (100 m isobath) since the extent of the 2023 bloom was not clear (or the bloom in any other year for that matter). The particles were prescribed to sink at 0.5 m/day, and hence were subject to the circulation deeper and deeper in the water column as time progressed. We documented where on the shelf each particle reached the BBL (taken to be 10 m above the bottom) or if it exited the shelf before doing so. The assumption is that turbulent BBL motions would bring the Chl *a* to the seafloor (see Section 3.4.1).

This calculation revealed that only a few particles reached the seafloor before being transported off the shelf, primarily through Barrow Canyon. The particles that grounded are marked in red in Figure 17c. There are some near the coast in the vicinity of Icy Cape that were in shallow enough water that they grounded before reaching Pt. Barrow. The three particles released near 72°N advected around Hanna Shoal and then entered a region of very weak flow before grounding just short of Barrow Canyon. The two particles released near 70°N in the western part of the domain grounded on top of Hanna Shoal. The main message here is that a substantial portion of Chl *a*, away from the front, likely exited the Chukchi shelf before reaching the bottom via gravitational sinking. This in turn highlights the importance of the frontal pumping mechanism in delivering carbon to the benthos.

To get an idea of the geographical extent of such a signature of enhanced sediment Chl *a* due to frontal pumping, we used the GLORYS12v1 hydrographic data to compute the magnitude of the lateral density gradient at 11 m

depth. We did this for each day of July 2023. The mean for the month is shown in Figure 17c. While there is a lot of structure, a clear signature of the front in question is evident extending from Central Channel, through the box, and on to Barrow Canyon (highlighted in the figure by hatching). This pattern is consistent from year to year, with small variations in the precise pathway, which implies that there should be a swath of enhanced carbon delivery on the northeast shelf. This in turn suggests that there may be a corresponding signature in benthic biomass. While there are known isolated benthic hotspots on the Chukchi shelf, for example, at the seaward end of the DBO3 line off of Pt. Hope (Grebmeier et al., 2015, 2018) and southeast of Hanna Shoal on the DBO4 line (Grebmeier et al., 2015; Schonberg et al., 2014), the resulting signature here might be more appropriately termed a benthic "hot region." It will be interesting to see if in situ measurements bear this out.

4. Summary

In June–July 2023, a field program conducted on R/V *Sikuliaq* documented the evolution of an under-ice phytoplankton bloom on the northeast Chukchi shelf. In this study, we used in situ data from the cruise, a simple numerical model, historical hydrographic and velocity data, and ocean reanalysis fields to characterize the physical setting and describe the dynamically driven vertical export of Chl *a* associated with the bloom.

A box was repeated seven times during the cruise which extended from within the ice pack in the north to open water in the south. The box bracketed a zonally oriented water mass front separating very cold, high-nutrient winter water in the north and warmer summer waters to the south—roughly coincident with the ice edge. The front supported a baroclinic jet which is part of the Central Channel flow branch that veers eastward toward Barrow Canyon. Using historical data, it was demonstrated that both the frontal jet and a barotropic jet located farther to the north are present throughout the summer and early fall, after the ice recedes, although the water masses on both sides of the front are warmer.

The phytoplankton bloom approximately doubled in strength over roughly a 2-week period while shifting farther into the ice pack, before beginning to decay and sinking at close to 0.5 m/day for roughly the following 2 weeks. In every occupation of the western and eastern sides of the box—the Hanna Ridge (HR) line and Hanna Ridge East (HRE) line, respectively—a plume of fluorescence extended downwards along the front toward the bottom. Using a regional numerical model and a passive tracer to represent the Chl *a*, it was demonstrated that the plume is the result of subduction due to baroclinic instability of the frontal jet. This process, in concert with the gravitational sinking, pumps the Chl *a* downwards at approximately 4 m/day, roughly an order of magnitude faster than the gravitational sinking alone.

A particle tracking calculation, using the ocean reanalysis fields for the summer of the cruise, was carried out to assess the ultimate fate of the phytoplankton in the bloom due to sinking alone. This revealed that a significant portion of the Chl *a*, away from the front, would be expected to be advected off of the northeast Chukchi shelf via Barrow Canyon before reaching the BBL. This highlights the importance of the frontal subduction process for delivering carbon to the sea floor. Since this process is ubiquitous each year—as demonstrated using the ocean reanalysis data—it should result in a swath of enhanced vertical carbon export which in turn should lead to increased benthic activity under the front. Notably, this process should be enhanced once the ice cover melts back, since ice-ocean friction tends to dampen the mesoscale instabilities driving subduction in these simulations. Hence, open water blooms on this part of the Chukchi shelf should experience even greater vertical export via this process.

Data Availability Statement

The shipboard CTD and water sample data used in the study are available at: https://doi.org/10.25740/pk659hh2169 (Van Dijken, 2024).

The historical hydrographic data are available from the following sources: (a) Unified Database for Arctic and Subarctic Hydrography (https://doi.pangaea.de/10.1594/PANGAEA.872931, Behrendt et al., 2018); (b) World Ocean Database 2018 (https://www.ncei.noaa.gov/products/world-ocean-database, Boyer et al., 2018); (c) Arctic Data Center (https://arcticdata.io/catalog/data, Lin et al., 2021); (d) Beaufort Gyre Exploration Project (https://www2.whoi.edu/site/beaufortgyre/data/data-overview, Proshutinsky et al., 2009); (e) Pacific Marine Environmental Laboratory (https://www.pmel.noaa.gov/data-links, Moore et al., 2018); (f) NOAA Alaska Fisheries

Science Center (https://data.eol.ucar.edu/dataset/, Danielson et al., 2020); (g) University of Alaska Fairbanks Institute of Marine Science (available at the Arctic Ocean Observing System, http://www.aoos.org, Danielson et al., 2020); (h) Fisheries and Oceans Canada's Institute of Ocean Sciences (https://www.dfo-mpo.gc.ca/science/publications/index-eng.htm, Danielson et al., 2020); (i) JAMSTEC (http://www.godac.jamstec.go.jp/darwin/e/, Itoh et al., 2013); and (j) Korea Polar Data Center (https://kpdcopen.kopri.re.kr, Jung et al., 2022).

The ChukSA climatology of shipboard ADCP, which includes the 2023 *Sikuliaq* data, are available from the NCEI repository: https://www.ncei.noaa.gov/access/metadata/landing-page/bin/iso?id=gov.noaa.nodc:0283043 (Bahr et al., 2023).

The GLORYS12V1 global ocean eddy-resolving reanalysis fields are available at https://doi.org/10.48670/moi-00021 (Lellouche et al., 2021).

References

Arrigo, K. R., Perovich, D. K., Pickart, R. S., Brown, Z. W., Van Dijken, G. L., Lowry, K. E., et al. (2012). Massive phytoplankton blooms under Arctic sea ice. *Science*, *336*(6087), 1408. https://doi.org/10.1126/science.1215065

Arrigo, K. R., & van Dijken, G. L. (2015). Continued increases in Arctic Ocean primary production. *Progress in Oceanography*, *136*, 60–70. https://doi.org/10.1126/science.aaf2671

Bahr, F., McRaven, L. T., & Pickart, R. S. (2023). ChukSA climatology, version 1.0: Ocean velocity profiles collected by ADCP in the Chukchi Sea, Bering Strait, and Bering sea in 2002–2022 (NCEI accession 0283043) [Dataset]. *NOAA National Centers for Environmental Information*. https://doi.org/10.25921/q8rx-9r22

Bannon, C. C., & Campbell, D. A. (2017). Sinking towards destiny: High throughput measurement of phytoplankton sinking rates through time-resolved fluorescence plate spectroscopy. *PLoS One*, *12*(10), e0185166. https://doi.org/10.1371/journal.pone.0185166

Behrendt, A., Sumata, H., Rabe, B., & Schauer, U. (2018). UDASH–unified database for Arctic and Subarctic hydrography. *Earth System Science Data*, *10*(2), 1119–1138. https://doi.org/10.1038/s41597-020-00539-9

Boyer, T. P., Baranova, O. K., Coleman, C., Garcia, H. E., Grodsky, A., Locarnini, R. A., et al. (2018). World Ocean database 2018 [Dataset]. *A.V. Mishonov, Technical Ed., NOAA Atlas 1015 NESDIS*. https://www.ncei.noaa.gov/sites/default/files/2020-04/wod_intro_0.pdf

Corlett, W. B., & Pickart, R. S. (2017). The Chukchi slope current. *Progress in Oceanography*, *153*, 50–65. https://doi.org/10.1002/2017GL074967

Danielson, S., Ahkinga, O., Ashjian, C., Basyuk, E., Cooper, L., Eisner, L., et al. (2020). Manifestation and consequences of warming and altered heat fluxes over the Bering and Chukchi Sea continental shelves. *Deep Sea Research Part II: Topical Studies in Oceanography*, *177*, 104781. https://doi.org/10.1038/s41558-019-0677-2

De Robertis, A., Taylor, K., Wilson, C. D., & Farley, E. V. (2017). Abundance and distribution of Arctic cod (Boreogadus Saida) and other pelagic fishes over the US continental shelf of the northern Bering and Chukchi seas. *Deep Sea Research Part II: Topical Studies in Oceanography*, *135*, 51–65. https://doi.org/10.1016/j.dsr2.2016.11.007

Eppley, R. W., Holmes, R. W., & Strickland, J. D. (1967). Sinking rates of marine phytoplankton measured with a fluorometer. *Journal of Experimental Marine Biology and Ecology*, *1*(2), 191–208. https://doi.org/10.1016/0022-0981(67)90043-4

Ershova, E. A., Hopcroft, R. R., Kosobokova, K. N., Matsuno, K., Nelson, R. J., Yamaguchi, A., & Eisner, L. B. (2015). Long-term changes in summer zooplankton communities of the western Chukchi Sea, 1945–2012. *Oceanography*, *28*(3), 100–115. https://doi.org/10.5670/oceanog.2015.61

Fang, Y. C., Weingartner, T. J., Dobbins, E. L., Winsor, P., Statscewich, H., Potter, R. A., et al. (2020). Circulation and thermohaline variability of the Hanna Shoal region on the northeastern Chukchi Sea shelf. *Journal of Geophysical Research: Oceans*, *125*(7), e2019JC015639. https://doi.org/10.1029/2019JC015639

Frey, K. E., Maslanik, J. A., Clement Kinney, J., & Maslowski, W. (2014). Recent variability in sea ice cover, age, and thickness in the Pacific Arctic region. *The Pacific Arctic region: ecosystem status and trends in a rapidly changing environment*, 31–63. https://doi.org/10.1201/b17466-3

Gong, D., & Pickart, R. S. (2016). Early summer water mass transformation in the eastern Chukchi Sea. *Deep Sea Research Part II: Topical Studies in Oceanography*, *130*, 43–55. https://doi.org/10.1016/j.dsr2.2015.06.007

Gorbunov, M. Y., & Falkowski, P. G. (2022). Using chlorophyll fluorescence to determine the fate of photons absorbed by phytoplankton in the World's oceans. *Annual Review of Marine Science*, *14*(1), 213–238. https://doi.org/10.1146/annurev-marine-040920-095522

Grebmeier, J. M., Bluhm, B. A., Cooper, L. W., Danielson, S. L., Arrigo, K. R., Blanchard, A. L., et al. (2015). Ecosystem characteristics and processes facilitating persistent macrobenthic biomass hotspots and associated benthivory in the Pacific Arctic. *Progress in Oceanography*, *136*, 92–114. https://doi.org/10.1016/j.pocean.2015.05.003

Grebmeier, J. M., Cooper, L. W., Feder, H. M., & Sirenko, B. I. (2006). Ecosystem dynamics of the Pacific-influenced northern Bering and Chukchi seas in the Amerasian Arctic. *Progress in Oceanography*, *71*(2–4), 331–361. https://doi.org/10.1016/j.pocean.2006.06.007

Grebmeier, J. M., Frey, K. E., Cooper, L. W., & Kędra, M. (2018). Trends in benthic macrofaunal populations, seasonal sea ice persistence, and bottom water temperatures in the Bering Strait region. *Oceanography*, *31*(2), 136–151. https://doi.org/10.5670/oceanog.2018.224

Hill, V., Ardyna, M., Lee, S. H., & Varela, D. E. (2018). Decadal trends in phytoplankton production in the Pacific Arctic region from 1950 to 2012. *Deep Sea Research Part II: Topical Studies in Oceanography*, *152*, 82–94. https://doi.org/10.1016/j.dsr2.2018.05.009

Hoskins, B. J., & Bretherton, F. P. (1972). Atmospheric frontogenesis models: Mathematical formulation and solution. *Journal of the Atmospheric Sciences*, *29*(1), 11–37. https://doi.org/10.1175/1520-0469(1972)029<0011:afmmfa>2.0.co;2

Itoh, M., Nishino, S., Kawaguchi, Y., & Kikuchi, T. (2013). Barrow Canyon volume, heat, and freshwater fluxes revealed by long-term mooring observations between 2000 and 2008. *Journal of Geophysical Research: Oceans*, *118*(9), 4363–4379. https://doi.org/10.1002/jgrc.20290

Jung, J., Lee, Y., Cho, K. H., Yang, E. J., & Kang, S. H. (2022). Spatial distributions of riverine and marine dissolved organic carbon in the Western Arctic Ocean: Results from the 2018 Korean expedition. *Journal of Geophysical Research: Oceans*, *127*(7), e2021JC017718. https://doi.org/10.1029/2021JC017718

Kuletz, K. J., Ferguson, M. C., Hurley, B., Gall, A. E., Labunski, E. A., & Morgan, T. C. (2015). Seasonal spatial patterns in seabird and marine mammal distribution in the eastern Chukchi and western Beaufort seas: Identifying biologically important pelagic areas. *Progress in Oceanography*, *136*, 175–200. https://doi.org/10.1016/j.pocean.2015.05.008

Lalande, C., Grebmeier, J. M., Hopcroft, R. R., & Danielson, S. L. (2020). Annual cycle of export fluxes of biogenic matter near Hanna Shoal in the Northeast Chukchi Sea. *Deep Sea Research Part II: Topical Studies in Oceanography*, *177*, 104730. https://doi.org/10.1016/j.dsr2.2020.104730

Lauer, J., van Dijken, G., Mills, M. M., Arlen, L., Zhong, G., & Arrigo, K. R. (2024). Export flux of ice Algae, under ice and open water phytoplankton in the Chukchi Sea. In *Proceedings of the American geophysical union, Ocean Sciences meeting*. 2715.

Lellouche, J.-M., Greiner, E., Bourdalle-Badie, R., Garric, G., Melet, A., Drévillon, M., et al. (2021). The Copernicus global 1/12° oceanic and sea ice GLORYS12 reanalysis. *Frontiers in Earth Science*, *9*, 585. https://doi.org/10.3389/feart.2021.644437

Lin, P., Pickart, R. S., McRaven, L. T., Arrigo, K. R., Bahr, F., Lowry, K. E., et al. (2019). Water mass evolution and circulation of the northeastern Chukchi Sea in summer: Implications for nutrient distributions. *Journal of Geophysical Research: Oceans*, *124*(7), 4416–4432. https://doi.org/10.1029/2018JC014593

Lin, P., Pickart, R. S., Våge, K., & Li, J. (2021). Fate of warm Pacific water in the Arctic basin. *Geophysical Research Letters*, *48*, e2021GL094693. https://doi.org/10.1029/2021GL094693

Logerwell, E., Busby, M., Carothers, C., Cotton, S., Duffy-Anderson, J., Farley, E., et al. (2015). Fish communities across a spectrum of habitats in the Western Beaufort sea and Chukchi Sea. *Progress in Oceanography*, *136*, 115–132. https://doi.org/10.1016/j.pocean.2015.05.004

Lowry, K. E., van Dijken, G. L., & Arrigo, K. R. (2014). Evidence of under-ice phytoplankton blooms in the Chukchi Sea from 1998 to 2012. *Deep Sea Research Part II: Topical Studies in Oceanography*, *105*, 105–117. https://doi.org/10.1016/j.dsr2.2014.03.014

Lu, K., Weingartner, T., Danielson, S., Winsor, P., Dobbins, E., Martini, K., & Statscewich, H. (2015). Lateral mixing across ice meltwater fronts of the Chukchi Sea shelf. *Geophysical Research Letters*, *42*(16), 6754–6761. https://doi.org/10.1002/2015GL064351

Marshall, D. (1997). Subduction of water masses in an eddying ocean. *Journal of Marine Research*, *55*(2), 201–222. https://doi.org/10.1357/0022240973224137

Marshall, J. C., Adcroft, A., Hill, C., Perelman, L., & Heisey, C. (1997). A finite-volume, incompressible Navier Stokes model for studies of the ocean on parallel computers. *Journal of Geophysical Research*, *102*(C3), 5753–5766. https://doi.org/10.1029/96JC02776

Marshall, J. C., Williams, R. G., & Nurser, A. G. (1993). Inferring the subduction rate and period over the North Atlantic. *Journal of Physical Oceanography*, *23*(7), 1315–1329. https://doi.org/10.1175/1520-0485(1993)023<1315:itsrap>2.0.co;2

Mastropole, D., Pickart, R. S., Valdimarsson, H., Våge, K., Jochumsen, K., & Girton, J. B. (2017). Hydrographic structure of overflow water passing through Denmark Strait. *Journal of Geophysical Research*, *122*(1), 306–321. https://doi.org/10.1002/2016JC012007

Moore, S. E., Grebmeier, J. M., & Giguère, N. (2018). The distributed biological observatory. *Arctic*, *71*, 1–7.

Moore, S. E., & Kuletz, K. J. (2019). Marine birds and mammals as ecosystem sentinels in and near Distributed Biological Observatory regions: An abbreviated review of published accounts and recommendations for integration to ocean observatories. *Deep Sea Research Part II: Topical Studies in Oceanography*, *162*, 211–217. https://doi.org/10.1016/j.dsr2.2018.10.008

Pacini, A., Moore, G. W. K., Pickart, R. S., Nobre, C., Bahr, F., Våge, K., & Arrigo, K. R. (2019). Characteristics and transformation of Pacific winter water on the Chukchi Sea shelf in late spring. *Journal of Geophysical Research: Oceans*, *124*(10), 7153–7177. https://doi.org/10.1029/2019JC015198

Pacini, A., Pickart, R. S., Bahr, F., Torres, D. J., Ramsey, A. L., Holte, J., et al. (2020). Mean conditions and seasonality of the west Greenland boundary current system near cape farewell. *Journal of Physical Oceanography*, *50*(10), 2849–2871. https://doi.org/10.1175/JPO-D-20-0086.1

Padman, L., & Erofeeva, S. (2004). A barotropic inverse tidal model for the Arctic Ocean. *Geophysical Research Letters*, *31*(2). https://doi.org/10.1029/2003GL019003

Perovich, D. K., & Polashenski, C. (2012). Albedo evolution of seasonal Arctic sea ice. *Geophysical Research Letters*, *39*(8). https://doi.org/10.1029/2012GL051432

Pickart, R. S., Lin, P., Bahr, F., McRaven, L. T., Huang, J., Pacini, A., et al. (2023). The Pacific water flow branches in the Eastern Chukchi Sea. *Progress in Oceanography*, *219*, 103169. https://doi.org/10.1016/j.pocean.2023.103169

Pickart, R. S., Moore, G., Mao, C., Bahr, F., Nobre, C., & Weingartner, T. J. (2016). Circulation of winter water on the Chukchi Shelf in early Summer. *Deep Sea Research Part II: Topical Studies in Oceanography*, *130*, 56–75. https://doi.org/10.1016/j.pocean.2011.03.001

Pickart, R. S., Pratt, L. J., Torres, D. J., Whitledge, T. E., Proshutinsky, A. Y., Aagaard, K., et al. (2010). Evolution and dynamics of the flow through Herald canyon in the Western Chukchi Sea. *Deep Sea Research Part II: Topical Studies in Oceanography*, *57*(1–2), 5–26. https://doi.org/10.1175/1520-0485(2002)032

Pickart, R. S., Spall, M. A., Lin, P., Bahr, F., McRaven, L. T., Arrigo, K. R., & Grebmeier, J. M. (2021). Physical controls on the macrofaunal benthic biomass in Barrow canyon, Chukchi Sea. *Journal of Geophysical Research: Oceans*, *126*(5), e2020JC017091. https://doi.org/10.1029/2020JC017091

Pickart, R. S., Spall, M. A., Moore, G. W., Weingartner, T. J., Woodgate, R. A., Aagaard, K., & Shimada, K. (2011). Upwelling in the Alaskan Beaufort sea: Atmospheric forcing and local versus non-local response. *Progress in Oceanography*, *88*(1–4), 78–100. https://doi.org/10.1016/j.dsr2.2009.08.007

Pickart, R. S., Torres, D. J., & Clarke, R. A. (2002). Hydrography of the Labrador sea during active convection. *Journal of Physical Oceanography*, *32*(2), 428–457. https://doi.org/10.1175/1520-0485(2002)032<0428:hotlsd>2.0.co;2

Pollard, R. T., & Regier, L. A. (1992). Vorticity and vertical circulation at an ocean front. *Journal of Physical Oceanography*, *22*(6), 609–625. https://doi.org/10.1175/1520-0485(1992)022

Proshutinsky, A., Krishfield, R., Timmermans, M.-L., Toole, J., Carmack, E., Mclaughlin, F., et al. (2009). Beaufort Gyre freshwater reservoir: State and variability from observations. *Journal of Geophysical Research*, *114*(C1), 1–25. https://doi.org/10.1029/2008JC005104

Ruiz, S., Claret, M., Pascual, A., Olita, A., Troupin, C., Capet, A., et al. (2019). Effects of oceanic mesoscale and submesoscale frontal processes on the vertical transport of phytoplankton. *Journal of Geophysical Research: Oceans*, *124*(8), 5999–6014. https://doi.org/10.1029/2019JC015069

Schonberg, S. V., Clarke, J. T., & Dunton, K. H. (2014). Distribution, abundance, biomass and diversity of benthic Infauna in the Northeast Chukchi Sea, Alaska: Relation to environmental variables and marine mammals. *Deep Sea Research Part II: Topical Studies in Oceanography*, *102*, 144–163. https://doi.org/10.1016/j.dsr2.2014.05.002

Schuback, N., Flecken, M., Maldonado, M. T., & Tortell, P. D. (2016). Diurnal variation in the coupling of photosynthetic electron transport and carbon fixation in iron-limited phytoplankton in the NE subarctic Pacific. *Biogeosciences*, *13*(4), 1019–1035. https://doi.org/10.5194/bg-13-1019-2016

Schuback, N., Tortell, P. D., Berman-Frank, I., Campbell, D. A., Ciotti, A., Courtecuisse, E., et al. (2021). Single-turnover variable chlorophyll fluorescence as a tool for assessing phytoplankton photosynthesis and primary productivity: Opportunities, caveats and recommendations. *Frontiers in Marine Science*, *8*, 690607. https://doi.org/10.3389/fmars.2021.690607

Shroyer, E. L., & Pickart, R. S. (2019). Pathways, timing, and evolution of Pacific winter water through Barrow canyon. *Deep Sea Research Part II: Topical Studies in Oceanography*, *162*, 50–62. https://doi.org/10.1016/j.dsr2.2018.12.003

Smagorinsky, J. (1963). General circulation experiments with the primitive equations: I. The basic experiment. *Monthly Weather Review*, *91*(3), 99–164. https://doi.org/10.1175/1520-0493(1963)091

Spall, M. A. (1995). Frontogenesis, subduction, and cross-front exchange at upper ocean fronts. *Journal of Geophysical Research*, *100*(C2), 2543–2557. https://doi.org/10.1029/94JC02825

Spall, M. A. (1997). Baroclinic jets in confluent flow. *Journal of Physical Oceanography*, *27*(6), 1054–1071. https://doi.org/10.1175/1520-0485(1997)027

Spall, M. A. (2007). Circulation and water mass transformation in a model of the Chukchi Sea. *Journal of Geophysical Research*, *112*(C5). https://doi.org/10.1029/2006JC003790

Springer, A. M., & McRoy, C. P. (1993). The paradox of pelagic food webs in the northern Bering Sea—III. Patterns of primary production. *Continental Shelf Research*, *13*(5–6), 575–599. https://doi.org/10.1016/0278-4343(93)90024-5

Stabeno, P. J., & McCabe, R. M. (2023). Re-examining flow pathways over the Chukchi Sea continental shelf. *Deep Sea Research Part II: Topical Studies in Oceanography*, *207*, 105243. https://doi.org/10.1016/j.dsr2.2023.105243

Thomas, L. N., & Joyce, T. M. (2010). Subduction on the Northern and Southern flanks of the Gulf Stream. *Journal of Physical Oceanography*, *40*(2), 429–438. https://doi.org/10.1175/2009JPO4187.1

Tian, F., Pickart, R. S., Lin, P., Pacini, A., Moore, G., Stabeno, P., et al. (2021). Mean and seasonal circulation of the Eastern Chukchi Sea from moored timeseries in 2013–2014. *Journal of Geophysical Research: Oceans*, *126*(5), e2020JC016863. https://doi.org/10.1029/2020JC016863

Van Dijken, G. (2024). Tale of three systems cruise data (SKQ202310S) [Dataset]. *Stanford Digital Repository*. https://doi.org/10.25740/pk659hh2169

Varela, D. E., Crawford, D. W., Wrohan, I. A., Wyatt, S. N., & Carmack, E. C. (2013). Pelagic primary productivity and upper ocean nutrient dynamics across Subarctic and Arctic Seas. *Journal of Geophysical Research: Oceans*, *118*(12), 7132–7152. https://doi.org/10.1007/s00300-008-0445-3

Weingartner, T., Aagaard, K., Woodgate, R., Danielson, S., Sasaki, Y., & Cavalieri, D. (2005). Circulation on the North central Chukchi Sea shelf. *Deep Sea Research Part II: Topical Studies in Oceanography*, *52*(24–26), 3150–3174. https://doi.org/10.1002/jgrc.20278

Weingartner, T., Cavalieri, D. J., Aagaard, K., & Sasaki, Y. (1998). Circulation, dense water formation, and outflow on the Northeast Chukchi shelf. *Journal of Geophysical Research*, *103*(C4), 7647–7661. https://doi.org/10.1029/2003JC001939

Weingartner, T., Fang, Y.-C., Winsor, P., Dobbins, E., Potter, R., Statscewich, H., et al. (2017). The summer hydrographic structure of the Hanna shoal region on the northeastern Chukchi Sea shelf: 2011–2013. *Deep Sea Research Part II: Topical Studies in Oceanography*, *144*, 6–20. https://doi.org/10.1002/2016JC012087

Woodgate, R. A., Aagaard, K., & Weingartner, T. J. (2005). A year in the physical oceanography of the Chukchi Sea: Moored measurements from autumn 1990–1991. *Deep Sea Research Part II: Topical Studies in Oceanography*, *52*(24–26), 3116–3149. https://doi.org/10.1029/JC090iC03p04509